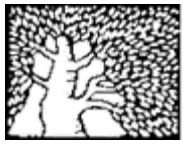

מכון ויצמן למדע

Weizmann Institute of Science

Thesis for the degree
Master of Science

By
Gili Assaf

חבור לשם קבלת התואר
מוסמך למדעים

מאת
גילי אסף

השוואת האפקטים הביופיסיקלים של פרוטונים וחלקיקי אלפא בעלי יוניזציה ממוצעת זהה על מולקולת הדנ"א

Comparison of the biophysical effects on DNA of protons and α-particles of equal mean ionization

Advised by
Prof. Amos Breskin

בהדרכת
פרופ. עמוס ברסקין

January 2003

שבט תשס"ג

Submitted to the Scientific Council of the
Weizmann Institute of Science
Rehovot, Israel

מוגש למועצה המדעית של
מכון ויצמן למדע
רחובות, ישראל

Abstract

The objective of this project is the study of the physical and biological effects related to the stochastic nature of radiation-induced energy deposition in matter, in nanometric scales.
The characterization of the biological effectiveness of ionizing radiation is currently evaluated by its LET value, corresponding to the mean ionization per unit length deposited at the cells' scales . However, it is now well recognized that the damage caused to the DNA molecule by stochastic radiation effects will determine the cell's chances of survival.
In this work we prove, for the first time, that equal-LET particles differ in their biological effectiveness. The reason for this difference lies in the nanometric structure of the particles' ionization patterns, of which the spatial density depends on the particle type and energy.
We base our research on the physical measurements of ionization patterns on nanometric, DNA-like, scales; we use a novel nanodosimetric experimental system developed in our group, measuring precisely the ionization in a small gas model of the DNA. In addition, we conduct direct biological measurements of the radiation-induced damage to plasmid DNA, in which we compare the type and amount of damage caused by the equal-LET particles. The experimental work is accompanied by extensive model-based simulations.
We may conclude that the degree of ionization clustering on DNA scales is the most relevant in the determination of the biological effectiveness of ionizing radiation.

Acknowledgments

I wish to express my deep gratitude to all of those who advised, supported and helped me to carry out this work.
In particular, I want to thank my advisor, Prof. Amos Breskin, whose expertise, commitment, support and encouragement were essential to me in the coarse of this project, and will inspire me always.
Special thanks to Dr. Rachel Chechik for insightful discussions and comments and to Guy Garty, Dr. Sergei Shchemelinin and Dr. Corinne Leloup who guided and escorted me in each step of my work; without their help this project would not have been completed.

I would like to extend special thanks:

To the accelerator team led by Prof. Michael Hass for their continuous commitment and assistance, and particularly to Yigal Shachar for his vast experience and exceptional help and support through long hours in the accelerator.

To Moshe Klin, Yafa Gil, Yehuda Asher and Shlomo Assayag for their extensive and valuable technical support.

To Prof. Bernd Grosswendt from PTB-Braunschweig, Germany, for his vast support and commitment regarding the MC simulations.

To Dr. Reinhard Schulte M.D. from Loma Linda University Medical Center, California, for useful discussions and advice.

To Prof. Elisha Moses' group for their help with the CCD camera and the frame-grabber card of the MCP setup.

To Michel Vidal-Naquet for the development of the MCP pictures analysis algorithm.

Finally, I would like to thank my dearest Noam and abba Pessach for their continuous love and encouragement.

Contents

1. Introduction

The study of the biological effects caused by ionizing radiation has become of prime importance in the last few decades, following the development in therapeutic medical applications, manned space flights and the need for radiation protection standards adapted to modern lifestyle.

The absorption of radiation in biological tissue causes ionizations and excitations of atoms and molecules within the cell, leading to the breakage of chemical bonds and creation of reactive species that proceed to react with the cellular constituents. Modern radiobiological research focuses on damage caused to the DNA molecule, recognized as the primary target for cellular inactivation [1, 2].

Chemical and biological effects of ionizing radiation depend not only on the dose (energy absorbed per unit mass), but also on the quality of the radiation, which in this context relates primarily to the spatial concentration of the primary collision processes along the charged particle track. The acceptable index used nowadays to describe radiation quality is the amount of energy lost per unit length of the track, i.e. the Linear Energy Transfer (LET). This factor provides an average of the rate of energy deposition at the micron level, making it limited to scales in the order of the cell diameter. However, the interaction mechanism of radiation with matter is a stochastic one; the damage to the cell will be caused by occasional, large locally-deposited energy at the nanometric DNA scale (e.g. end of δ-electrons track). Therefore, the specific structure of ionization events along the charge particle track will determine the severity of the induced damage (reparable or irreparable), i.e. the biological effectiveness of the radiation.

Radiation quality factors such as LET are well recognized as a general description of biological effectiveness [3]. However, with the recent development in technology and comprehension of biological processes, we are now able for the first time to measure the stochastic nature of energy deposition events at the DNA scale; we can compare the ionization effects of equal-LET particles on nanometric-equivalent scales, as well as their biological effectiveness on real DNA samples.

The goal of this work is to carry out such studies with protons and α-particles of equal LET. We would like to understand whether small variations in the primary and secondary (δ-electrons) energy deposition patterns would cause a significant difference in the biological effectiveness of the radiation. It is generally assumed that the difference in biological effectiveness of such particles are negligible [4]. This assumption implies that although there are known differences in the track structures at the nanometer level, these are not sufficiently large to be biologically significant. Up to date, due to the lack of experimental methods, there are no real measurements of the stochastic distribution of particle-induced ionization events on DNA-nanometric scales. There is only one evidence in the literature that low-energy protons may induce as much as twice the damage than α-particles of the same LET [5].

In this project we employ the novel experimental nanodosimetric system (ND) developed in our group, to measure the ion cluster-size distribution of 1.03 MeV protons and 26 MeV α-particles, both having LET value of 25.5 keV/μm, and in parallel, conduct biological experiments to study their effects on DNA.
The ND experimental system is a novel tool to measure ionization effects in small millimetric gas volumes, providing a million-times expended model of the DNA. The ionization measurements are preformed by counting single ions induced by the charged particles in low-pressure gas. Biological effectiveness studies have been carried out in parallel, through the irradiation and analysis of plasmid DNA. The experiments where conducted in the Pelletron and Van de Graaf accelerators of the Weizmann Institute, and required the assembly of a new RF ion source at the Pelletron, and a new beam line at the Van de Graaf.
Correlating the physical measurements with the biological measurements of cell mutation rates and DNA inactivation, would allow us to investigate the significant characteristics that will determine the biologically-relevant quality factors of ionizing radiation. The ability to better characterize the biological effects of ionizing radiation would open new opportunities in the development of new radiation protection standards and radiation therapy planning.
A major part of the decision-making process in this project was based on extensive simulations of the energy deposition and ion-counting processes occurring within our experimental system. Through such simulations we were able to explore the effects of primary and secondary radiation processes, and to choose the optimal experimental conditions.
A Monte Carlo code simulated the track structure of the ionizing radiation in the gas, and was accompanied by another code, which simulated the ion collection efficiency by the ion counter. The good agreement between the simulated and the measured results allowed us to use the simulations in order to isolate problematic issues in the experiment, understand the processes occurring in each step, and debug our system accordingly. Consideration of energy straggling and scattering of the charged particles as they pass through different materials where also based upon simulations.
Another important experimental issue was the choice of a particle trigger detector. Its role being of providing an efficient trigger to the nanodosimeter data acquisition system, as well as relevant information about the particle beam uniformity. We were also in need for a detector that measures the energy spectrum of the particle beam.
Several types of particle detectors were investigated. A prototype MWPC was designed, built and characterized. Conditions were found, allowing to detect 4 MeV α-particles at 0.9 Torr gas pressure, at which the ND operates. A solid-state detector system gave us the possibility to inspect the beam energy spectrum at every stage of the experiment. A vacuum-operated micro channel plate (MCP) detector system with a phosphor screen viewed by a CCD camera was assembled and used both as trigger and as a monitor of the beam's uniformity and size, crucial to our experiments.
In the following chapters I will provide the scientific background related to ionizing radiation research, describe the physical and biological experimental techniques and discuss the simulation's contribution to this project. Finally, the results of both physical and biological measurement will be presented, comparing the various differences between equal LET protons and α-particles. The report will be concluded with some views to the future.

2. Theoretical background

2.1 Radiation damage to DNA

The DNA molecule, shown schematically in figure 2.1, consists of two polynucleotide chains wound around each other in a right-handed double helix. The strands are made up of subunits called nucleotides, each containing a sugar (deoxyribose), a phosphate group, and one of four nitrogenous bases - adenine, guanine, thymine, and cytosine, denoted A, G, T, and C, respectively.
The DNA is considered to be the primary target molecule for radiation damage [1, 2]. The most commonly observed damage to the DNA following irradiation is the presence of base damage (BD), single-strand breaks (SSBs) and double-strand breaks (DSBs). Base damage occurs when the chemical properties of the nitrogenous base are abnormally modified, SSBs are formed where the covalent bond between the deoxyribose sugar unit and the phosphate group is broken. Two SSBs on opposite strands, separated by a small number of nucleotide pairs will result in a DSB, considered to be the most hazardous to cell functioning [6, 7].
Damage induced in the DNA is subject to a series of enzymatic processes that may either lead to a successful repair or to the fixation of damage (i.e. misrepair) [8, 9]. Such mechanisms usually consist of enzymatic "proofreading" of the DNA double helix, identifying mismatched

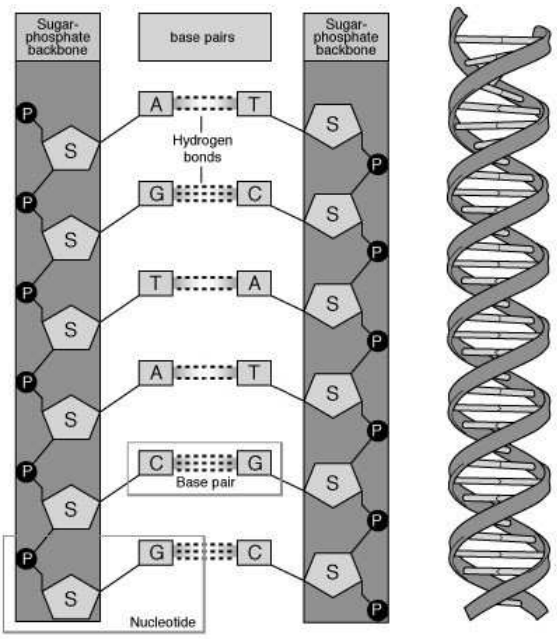

Fig. 2.1: *Schematic diagram of the DNA molecule; the sugar-phosphate backbones are on the outsides of the double helix, while the bases are oriented toward the central axis. Each spiral strand is connected to a complementary strand by non-covalent hydrogen bonding between paired bases. Adenine and thymine are connected by two hydrogen bonds while guanine and cytosine are connected by three.*

pairs and distorted molecules, followed by excision of the damaged segment, while relying on the information present in the complementary DNA strand to replace it. Usually, SSBs damage can be successfully repaired, while the repair of damages resulting in multiple lesions to both strands (i.e. DSBs), may induce large genetic alterations, affecting gene expression and in some cases, cell survival [10].
The damage to DNA is generally considered to arise from two different sources: the direct and indirect effects. Direct effect damage originates from energy deposited in the DNA molecule itself; the indirect effect arises following attacks on the DNA by reactive species, produced by ionization of other molecules in its surroundings. The major source of indirect effects is the production of free radicals and active oxygen species from water molecules [11]. Free radicals are highly reactive molecules with an unpaired electron. The presences of scavengers (any chemical species that interact with the radicals) limits their life time to approximately 10^{-9} sec [12], allowing the radicals to diffuse in the cell over a distance of a few nm; thus, if the radicals are created close enough to the DNA, they interact with the molecule and produce damages similar to those occurring from the direct effect. The radiolysis of water may be described by the following reaction sequences [13, 14]:

$$\begin{aligned} irradiation\ of\ H_2O &\longrightarrow H_2O^+ + e^- \\ followed\ by: & \\ H_2O + H_2O^+ &\longrightarrow {}^\bullet OH + H_3O^+ \\ H_2O + e^- &\longrightarrow H^\bullet + OH^- \\ {}^\bullet OH + {}^\bullet OH &\longrightarrow H_2O_2 \\ H^\bullet + H^\bullet &\longrightarrow H_2 \end{aligned}$$

Thus the initial species produced on water radiolysis are written as:

$$H_2O \rightsquigarrow {}^\bullet OH, H^\bullet, H_2O_2, H_2, H_3O^+$$

The radiolysis products are believed to be responsible for about 65% of all biological damage, while the other 35% are caused by direct ionization of the DNA molecule [11, 15].

2.2 Interaction of charged particles with matter

Energetic charged particles lose kinetic energy to their environment through coulomb-interactions with the electrons of the medium. The energy transferred in the interaction depends on the charge of the particle and its velocity, which causes a dramatic rise in the rate of energy transfer per unit path-length as the particle approaches the end of its path, where its kinetic energy approaches zero. An expression for the average energy-loss per path-length due to coulomb interactions has been obtained by Bethe and Bloch:

$$-\frac{dE}{dx} = \frac{4\pi z^2 e^4}{m_0 c^2 \beta^2} NZ \left[ln \frac{2m_0 c^2 \beta^2}{I(1-\beta^2)} - \beta^2 \right] \qquad \text{ergs/cm} \tag{2.1}$$

Where ze is the charge of the particle, β is the ratio of its velocity to the speed of light, N and Z are the number density and atomic number of the absorber's atoms; m_0 is the electron rest mass and I represents the effective excitation and ionization potential of the absorber.

This formula defines the average rate of energy transfer to the medium, known as the Linear Energy Transfer (LET) of the radiation. LET is closely related to the radiation's ability to produce biological damage and is widely used to qualify different types of radiation for radiobiological purposes [3]. Radiation can be classified either as "low LET", causing relatively low damage (gamma-rays such as ^{60}Co and ^{137}Cs or X-rays, which have mean LET value of 0.2-3 keV/μm), or as "high LET" (low-energy protons, α-particles and other heavy charged particles, having LET values higher then 100 keV/μm), considered to be biologically harmful. However, since LET can only characterize the **mean energy** deposited in a given volume, it contains no information about the **stochastic** distribution of energy deposition events, which is believed to be of great importance for determining the biological effectiveness of ionizing radiation [16].

2.2.1 The production of δ-electrons

In the ionization process, the ejected electrons' energy can reach values up to the maximal energy allowed to be transferred in each interaction. Electrons ejected with energy above few tens of eV are normally called δ-electrons; these electrons carry sufficient energy to further ionize the medium, inducing secondary ionization tracks. A typical simulated fraction of a charged-particle track is shown in figure 2.2. The δ-electrons represent additional means by which the charged particle's energy is transferred to the medium, creating a halo of secondary ionizations around the primary particle track. The angle of emission of δ-electrons of energy E is given, in a free-electron approximation, by the expression [17]:

$$cos^2\,\theta = \frac{E}{E_m} \tag{2.2}$$

Where E_m is the maximal energy allowed for the δ-electrons. Most δ-electrons are emitted perpendicular to the incident track [18]; however, multiple scattering in the medium quickly randomizes the direction of their motion, causing them to ionize the medium in a stochastic manner [19], thus producing **clustered-ionizations**, which could cause lethal damage to the DNA.

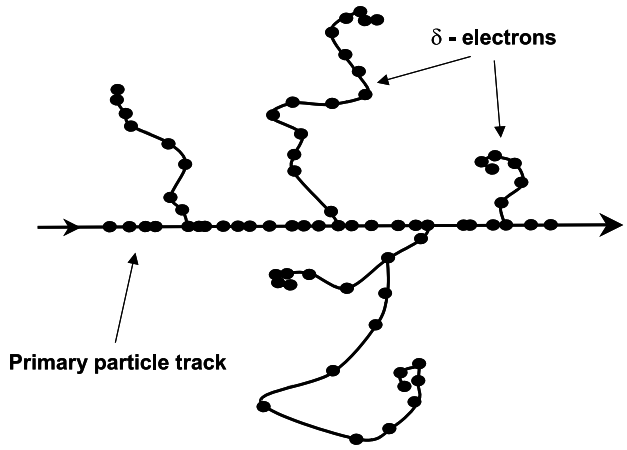

Fig. 2.2: *A simulated fraction of a typical charged-particle ion track. The range of the δ-electrons is always very small compared to that of the incident primary particle; yet, they are responsible for almost half of the ionizations occurring in the medium.*

2.3 Microdosimetry and Nanodosimetry

The objective of microdosimetric studies is the development of concepts to investigate the principle features of the stochastic absorption of ionizing radiation in matter, at the micrometeric scale, i.e. that of the cell.
Experimental **microdosimetry**, developed by Harold Rossi and his colleagues in the mid-fifties, suggests the use of low-pressure tissue-equivalent gas proportional counters (TEPC) [20]; These instruments, consisting of an "expanded gas model" of the cell (see below), have versatile uses in radiation physics, radiation protection and radiation biology.
Nanodosimetry is a natural extension of microdosimetry into the nanometer-scales domain. Its role is investigating stochastic ionization effects at the nanometric scales, i.e. that of the DNA, which are accepted as more relevant to radiation damage. The aim of the nanodosimetric studies is to measure the stochastic nature of the track structure of charged particles, and, with appropriate models, predict the biological effectiveness of particles of different types and energies.
In Nanodosimetry, the relevant targets are cylinders of 2-4 nm diameter and 16 nm length, corresponding to short segments of the DNA molecule (about 50 base-pairs) and its surrounding water layer [21, 22]. In order to simulate such conditions realistically, one has to create a relatively large ionization volume in which a much smaller, ideally wall-less sensitive volume is embedded. Radiation-induced charges produced within the core of the sensitive volume should be collected with high efficiency, simulating the direct ionization of the DNA itself, while charges produced in the periphery of the volume should be collected with an efficiency that falls off in a distance-dependent manner, simulating the indirect radiation effect in which free radicals of water radiolysis react with DNA molecule.

2.3.1 Modelling in gas

The accepted method to experimentally determine the energy deposition patterns in microscopic volumes of condensed matter (biological tissue), is simulating them by a much larger cavity, filled with tissue-equivalent gas (TEG).
The principle of tissue-equivalence rests upon the empirical observation that the transfer of radiation energy from charged particles depends primarily on the atomic composition of the absorber, regardless of the actual chemical combination of its constituents [23, 24]. Since we are interested in modelling the DNA molecule and its surrounding (mostly liquid water), the tissue-equivalent gases should contain elements of tissue and water, namely H, C, N and O. Common TEGs used in radiation studies are propane-based (composed of C_3H_8, CO_2 and N_2) and methane-based (composed of CH_4, CO_2 and N_2). In our experiments we are using pure propane - C_3H_8. If we demand that the number of primary-particle interactions should be the same in both materials, we can introduce a dimensional scaling factor for the gaseous model:

$$\rho_t \Delta X_t = \rho_g \Delta X_g \tag{2.3}$$

Where $\rho_{t,g}$ is the density of the tissue and gas, respectively, and $\Delta X_{t,g}$ is the scale in the respective medium.

Thus, the gas substitution of a microscopic tissue volume is possible if the product of the gas density and the gas cavity diameter is equal to that of the tissue volume diameter and density, and that the cross-sections for ionizations are independent of the medium density. However, this scaling factor should be considered only as a first order approximation, since tissue-equivalent gases and tissue do not have identical atomic composition, therefore one cannot assume that the interaction cross-sections in both cases are identical.
Furthermore, other definitions of gas and tissue equivalence are possible. For example, we can demand that the energy loss ΔE of the primary particles should be the same in both materials, thus including the mass stoping powers (which depend on particle type and energy) in the scaling factor formula. Another complication is due to secondary ionization processes (induced by δ-electrons), which have very different cross-sections compared to the primary ionization processes, requiring considerations of different scaling factors for the electron-induced ionizations.
However, a research done recently by one of our colleagues [25], claims that the properties of liquid water are largely similar to those of propane-based tissue-equivalent gas; therefore measurement preformed in such gas can be used to estimate the size of ionization clusters formed in nanometric volumes of liquid water.
Since we are not trying to claim one to one correspondence between tissue and gas, but rather develop a model connecting the ionization effects in gas to those induced on the DNA, the scaling factor in (2.3), resulting in the scaling of 2.1 nm in tissue to 1 mm in gas, serves as a good approximation for the purpose of our study.

2.3.2 Charge counting dosimetry

The experimental nanodosimetry technique, developed at our group [26, 27, 28], is shown schematically in figure 2.3. It is based on extraction and counting of single charges created in a pre-defined wall-less sensitive volume.
This charge counting technique is based on the conversion, in a low-pressure gas, of ionizing radiation into a cluster of charges. The deposited charges (ions) are extracted from the interaction region by an electric field E_1, into a vacuum region, where they are individually detected by a vacuum based electron multiplier.
By counting the number of ions we are able to determine the original ionization density, with a resolution of up to 1 mm, dictated by the ions diffusion in the gas. We can thus measure precisely the ionization density in very dilute gases and determine the location of each deposited charge, with an equivalent resolution of few nanometers.

2.3.3 Formation of the sensitive volume

The sensitive volume equivalent size has great conceptual importance; it should correspond to the size of the structures desired to be modelled, i.e. a short DNA segment and its surrounding water layer. The sensitive volume is formed by a gas region from which ions can be extracted through a small aperture, with a certain efficiency. Its tissue-equivalent size depends on the gas type and density, on the applied electric fields and the ion-extraction aperture size. The ions are extracted into vacuum (obtained by a differential pumping system), multiplied, detected and counted. The arrival time of the ions enables determining their original location along the

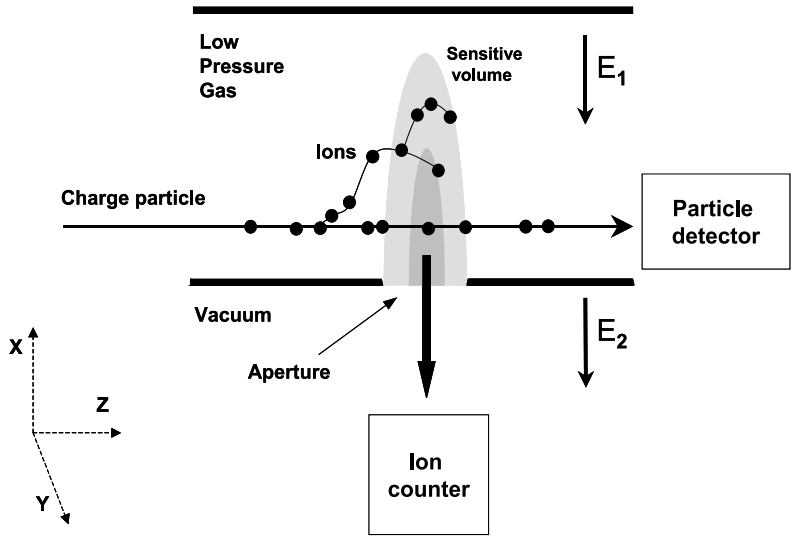

Fig. 2.3: *A schematic diagram of the ion-counting nanodosimeter; ions generated in gas-filled ionization volume by a single charged particle are extracted from the sensitive volume into vacuum, where they are accelerated and individually recorded by an ion counter.*

X coordinate (see figure 2.3), while the Y and Z coordinates are determined by the aperture location relative to the ionizing particle track. The extraction efficiency is diffusion-limited; it drops with increased distance from the aperture.

2.4 Broad beam irradiation

In order to correlate between biological and physical experiments we must work in the appropriate biological conditions, where there is no spatial correlation between the radiation track and the biological target, meaning that the biological target (usually of the size of a few tens of nm^3, corresponding to a short segment of DNA and its surrounding water layer) is exposed to a spatially uniform irradiation field; therefore, in our experiment, we must use a relatively broad beam, taking the beam diameter to be larger than the size of the modelled target volume by the effective range of δ-electrons in our current experimental conditions (a larger beam would not induce any additional ions in the target volume). This range can be extracted from the Monte Carlo simulation of the track structure for each radiation type. A detailed description of this procedure can be found in section 4.1.

2.5 Choosing the energies of the equal-LET particles

The energies of the equal LET protons and α-particles at which the experiments were conducted, were chosen according to the particle energies range available at the Pelletron and Van de Graaf accelerators in the Weizmann Institute. A new RF source was purchased for the purpose of our measurements, and assembled in the Pelletron accelerator, able to produce 12-36 MeV α-particles. The experimental system was then moved to the Van de Graaf accelerator (capable to produce 0.1-2.5 MeV protons), where a new beam line was assembled.

The exact energies of the particles had to fulfil two requirements: First, due to the structure of the experiments, the particles were passed through several scattering foils before reaching the sensitive volume, resulting in energy straggling; thus, their initial energy had to be higher than the desired energy for our measurements, while being in the stable region of the accelerator's available energy range. Secondly, the protons' energy had to be as high as possible in order to minimize scattering and energy degradation of the particles. Thus, we have taken the upper limit available for the α-particles in the Pelletron, which resulted in an energy of 26 MeV inside the sensitive volume, having LET value of 25.5 keV/μm. The corresponding protons of equal LET are of energy 1.03 MeV, requiring the VdG accelerator beam to have an initial energy of about 2 MeV. Figure 2.4 gives the LET values in water of protons and α-particles in the range of interest, as a function of their energy.
Similar comparison was previously done only once, by Goodhead *et al.*(1992), who compared the biological effectiveness of protons and α-particles with LET values between 20-23 keV/μm, by irradiating mammalian cells and analyzing their survival curves. His findings were that protons are up to twice more effective in causing biological damage than the α-particles [29].

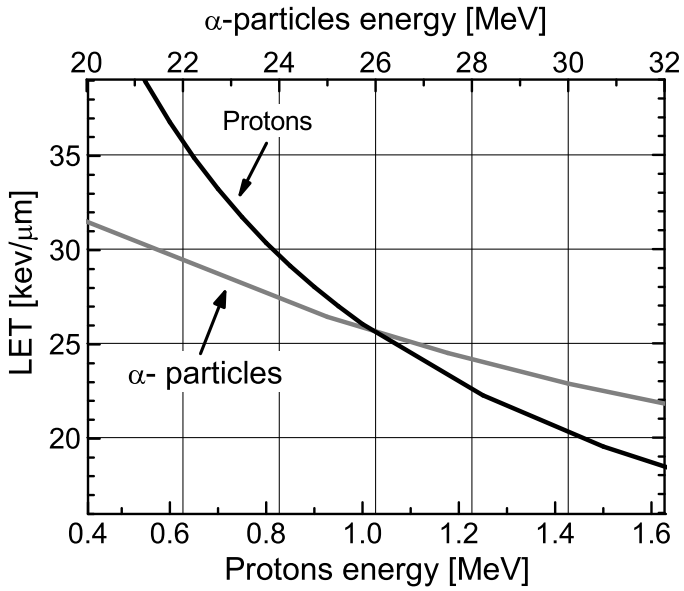

Fig. 2.4: *The LET in water of protons and α-particles as a function of their energy. At LET value of 25.5 keV/μm, the particles' energies are 1.03 MeV and 26 MeV, respectively.*

3. Experimental techniques

3.1 The ion-counting nanodosimeter - Physics experiments

3.1.1 The nanodosimeter structure

A detailed view of the ion-counting nanodosimeter (ND) is shown in figure 3.1. A charged-particle beam traverses the ionization volume and reaches a trigger detector. Ions induced in a wall-less sensitive volume (SV) within the ionization volume, are extracted into the vacuum-operated detection volume and detected by an ion counter. For each triggered primary-particle event, the data acquisition system (DAQ) registers both the number and the arrival time of the ions with respect to the trigger. The ionization volume contains a low-pressure (0.9 Torr) propane gas at a density of $2 \cdot 10^6$ g/cm^3. Under these conditions, 1 mm in gas corresponds to 2.1 nm in condensed matter (see section 2.3.1). The ions are drifted and extracted through a 1 mm circular aperture into the intermediate vacuum region (10^{-3} Torr) via the electric fields E_1 and E_2, and accelerated into the ion detection volume ($3 \cdot 10^{-5}$ Torr). The pressure difference between the ionization volume and the detection volume is achieved by a double differential pumping system, consisting of two turbomolecular pumps.

The ionization volume

The ionization volume is enclosed in a stainless-steel vessel of 150 mm diameter (much larger than the few-mm diameter sensitive volume). The electric field E_1 is shaped by an aluminum anode, placed 50 mm above the grounded cathode encompassing the ion-extraction aperture. Additional field shaping electrodes ensure field uniformity.

The value of E_1 is used to tune the length of the sensitive volume. However, it was measured that when E_1 is larger than 40 V/cm at 0.9 Torr propane, multiplication processes begin (the electrons that were created in the ionization process induce further unwanted ionizations on their way to the anode, generating additional ions in the gas). In order to eliminate this effect, while preserving high ion collection efficiency, we apply a pulsed electric field E_1, using a high voltage pulser; during steady state conditions, E_1 is kept at about 20 V/cm (below the gas multiplication threshold but sufficiently high to sweep away particle-induced electrons within one or two microseconds). Five microseconds after the beam particle trigger, the field E_1 is raised to the desired value of 60 V/cm for 180 μs, required for full ion clearing.

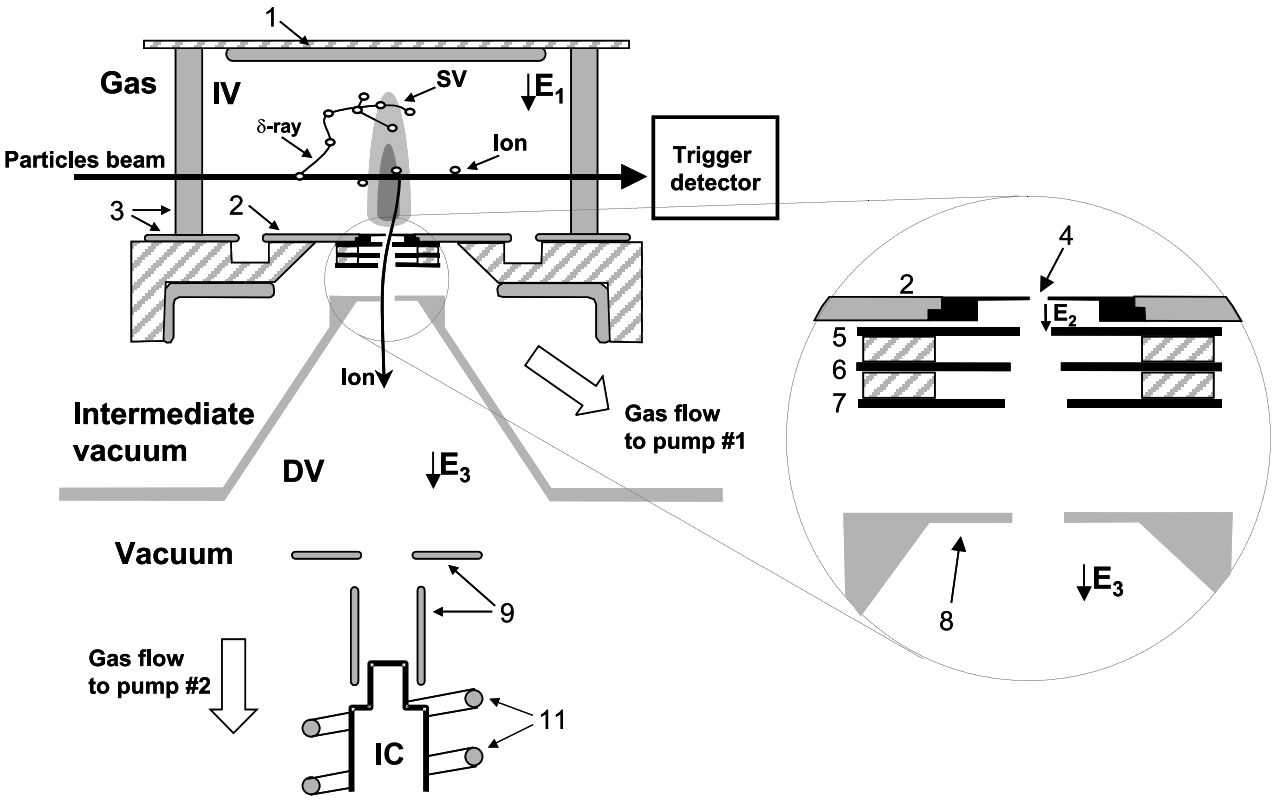

Fig. 3.1: *A detailed diagram of the ion counting nanodosimeter. In the ionization volume (IV), the anode (1), cathode (2) and field shaping electrodes (3) determine the extraction field E_1. Ions created within the sensitive volume (SV), are extracted via the aperture (4) into the intermediate vacuum region; they are focused under the field E_2 via the electrodes (5, 6, 7 and 8) into the detection volume (DV), where they are accelerated and focused, by the electrodes (9) into the ion counter (IC). A helical coil (11) protects the ion counter from discharges. Note that the SV and δ-ray are schematic representations and not to scale.*

The sensitive volume

The size and shape of the wall-less sensitive volume (SV) embedded into the ionization volume are determined by the transport of ions in the gas and their extraction efficiency through the aperture. By varying the gas density, the aperture diameter as well as the electric field E_1 above the ion extraction aperture and E_2 below it, we can tune the SV shape and size. In the current conditions the SV has a cylinder-like shape, which simulates the desired nanodosimetric site of a DNA segment and its surrounding water layer.

The SV may be represented by a map of iso-efficiency contours, corresponding to equal ion extraction efficiencies (figure 3.2). These maps are calculated with a Monte Carlo simulation, taking into account the electric field geometry in the ND and the measured transport parameters of propane ions [30].

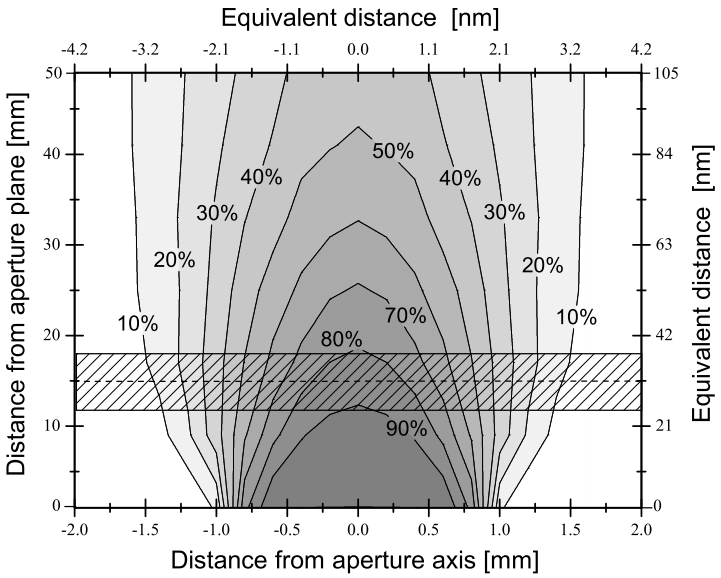

Fig. 3.2: *Monte-Carlo simulated map of the ion extraction efficiency, defining the wall-less sensitive volume (SV). Each contour line represents a change of 10% in the extraction efficiency. The dashed line 15 mm above the aperture shows the center of the beam course through the SV, while the marked area around it is the biologically-relevant volume corresponding to a short segment (16 nm) of a DNA molecule and its surrounding water layer (note that the vertical scale is about 15 times larger then the horizontal scale for better visualization of the SV). The bottom and left scales are real distances in gas, while the top and right scales provide the equivalent distances in nanometers. The SV shown corresponds to an electric field configuration of $E_1 = 60$ V/cm and $E_2 = 1100$ V/cm.*

The detection volume

Three gold-plated electrodes with a central opening are located immediately below the ion-extraction aperture and serve as ion-focusing electrodes. The purpose of these electrodes is to generate the focusing field E_2 near the aperture and to guide the ions extracted from the ionization volume into the detection volume (the potentials on these electrodes as well as on the electrodes in the ionization volume were optimized to yield maximum ion collection efficiency). Within the evacuated detection volume, ions are accelerated onto a discrete dynode electron multiplier (EM), whereby they are individually detected and counted. The signal is read out from the last dynode of the EM via an induction coil; it is then amplified and shaped using a fast preamplifier followed by a timing filter amplifier. The resulting pulses are 20 nsec wide and reach amplitudes of up to 600 mV with a noise level of 16 mV. Single ion pulses and typical pulse trail from the ion counter are shown in figure 3.3.

DAQ system and analysis

The data acquisition system (DAQ) correlates between the projectiles and their corresponding ions, registering the arrival time of each ion with respect to the trigger. In the offline analysis, the validity of each event is checked against strict triggering requirements. Relevant events are

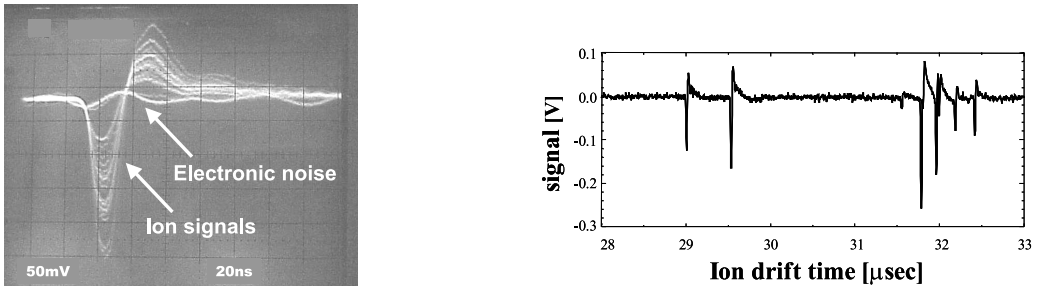

(a) (b)

Fig. 3.3: *(a) Photo of single ion pulses from the ion counter. (b) Ion pulse train induced in the SV by a single α-particle.*

selected and appropriate histograms are generated. Of particular interest are the cluster-size and arrival times distributions of the ions. The latter provide important information on the spatial distribution of ions relative to the projectile's trajectory. A typical ion drift velocity in our conditions is about 0.4 mm/μs, resulting in ion drift times of 20-40 μs, depending on where the ion was created above the aperture. This poses a limitation on the maximal possible beam rate; in order to avoid counting ions from two or more projectiles within the same cluster (pile-up), we usually require a delay of 200 μs between consecutive projectiles. In the offline analysis, we first perform the pile-up rejection, namely rejecting all triggering events that are followed or preceded by another event within less than 200 μs.
From each dataset, typically of $2{\cdot}10^6$ non-overlapping collimated events (measured over a period of 2-3 hours, at beam rates of a few hundreds particles per sec), we generate an ion cluster-size spectrum; it provides the frequency at which clusters of a given number of ions are induced within the SV by a single ionizing particle. For the purpose of relating the ion cluster-size distribution to the biological effectiveness of the radiation, we must normalize the distribution without the frequency of the "empty" (or "zero") clusters, which have no biological significance since no damage is induced.
The ion arrival time distribution is correlated with the initial ion deposition location along the SV axis, meaning its distance from the extraction aperture. This information may be used to measure the ionization density profile across the particle's track, and examine the radiation field uniformity (a uniform field throughout the SV would yield flat arrival time distribution. See figure 3.4). It can also be used to subdivide the data into selected time windows, equivalent to the division of the SV length into small segments, a few nanometers long. This is possible due to the rather small ion diffusion in the gas (about 1 mm for every cm drift), meaning that the information on the initial ion deposition distance is well preserved, with a resolution of a few nm. Thus, we can use the time-cut analysis selection tool to define a biologically relevant volume, which is a 7.6 mm high cylinder, corresponding to a short segment (16 nm) of the DNA double helix, from which the ions are collected (see fig. 3.2).
The experimental results are accompanied by a Monte Carlo simulation, based on measured ionization cross-sections of charged particles in propane [31]. A detailed description of the various calculations done with the simulation, and their importance to our experiments are

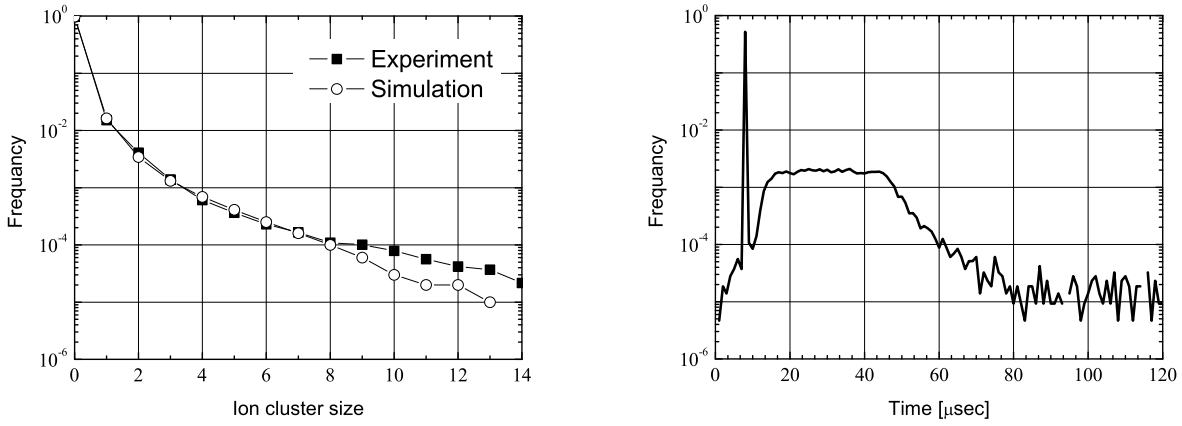

(a) Ion cluster size

(b) Ion arrival time

Fig. 3.4: *Ion cluster size distribution (a) and arrival time distribution (b) of 19.3 MeV protons with beam diameter of 20 mm. The SV is exposed to a uniform irradiation field, causing the arrival time distribution to be flat (The peak at 10 μsec is due to pickup from the pulser).*

given in chapter 4. Figure 3.4 shows the measured and simulated ion cluster size distributions and the measured ion arrival time distribution of 19.3 MeV protons with beam diameter of 20 mm (uniform irradiation).
More details about the ND, the DAQ system and the model used for the MC simulations are given in our recent article [26].

3.1.2 Accelerator beam setup

The nanodosimeter was operated in the Pelletron accelerator for the measurements of high energy protons (7-20 MeV) and 26 MeV α-particles, and was then moved to the Van de Graaf accelerator for the 1.03 MeV protons measurements. The beamline setup in both locations is shown in figure 3.5. The accelerator beam is scattered by a thin foil, covered by a 1 mm aperture collimator; the foil's thickness is chosen according to the particle type and energy, yielding no more then a few percent difference in the beam flux throughout the entire beam diameter, while causing relatively small energy straggling (we used a 50.8 μm stainless-steel foil for the 26 MeV α-particles and a 0.5 μm Au foil for the 1.03 MeV protons). After passing through a series of 20 mm collimators (set to prevent particles scattered from the pipe edges to reach the SV), the beam is cut down to the desired diameter by a smaller collimator. The collimated beam enters the ND gas volume through a thin Mylar foil (2.5 μm), passes through the SV (centered at 15 mm above the aperture), and reaches the trigger detector, separated from the ionization volume by a similar foil.
In these experiments, the trigger detector used is a double multi channel plate detector (MCP) coupled to a phosphor screen and a CCD camera. Fast pulses from the MCP anode are used

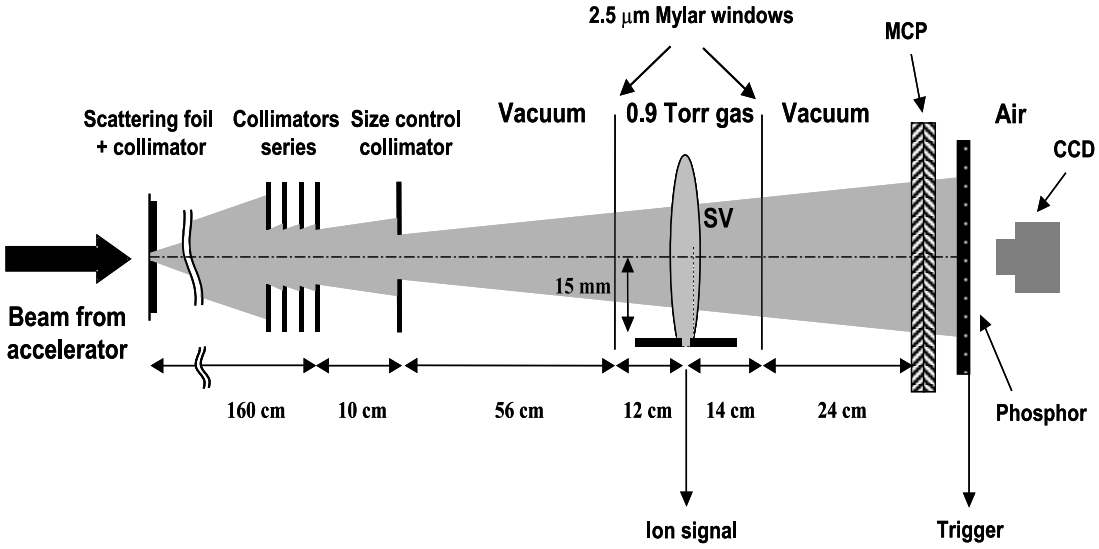

Fig. 3.5: *Accelerator beam-line configuration. See text.*

to trigger the ND while the beam geometry and uniformity can be monitored by the picture obtained from the phosphor screen. A broader discussion on beam uniformity is given below.

3.1.3 Broad beam irradiation

The diagnostics and optimization of the ND was carried out using a pencil beam of 1 mm diameter [26]. Yet, for simulating real biological conditions, we must expose the biologically relevant volume (see figure 3.2) to a uniform irradiation field, preventing any spatial correlation between the radiation track and the biological target.
The ideal situation is irradiation with an infinite beam diameter. However, since it is not experimentally realistic, we have found, using the MC simulations, that when working with a beam diameter of 20 mm, in the case of high-energy protons and α-particles, we can expect only 6% difference in the uniformity of the irradiation, compared to the irradiation with an infinite beam, and only 3% difference for the 1.03 MeV protons. A detailed discussion on this matter is given in section 4.1
The ions induced in the biologically relevant volume (chosen by the time-cut analysis) are the best representation of the stochastic ionization patterns created in a short segment of the DNA molecule.

3.1.4 Triggering detectors

The operation of several possible triggering detectors was investigated in order to get maximal detection efficiency of the charged particles and gain important information about the beam quality such as energy spectrum, size, shape and spatial uniformity. The following section describes the operation of a dedicated prototype multiwire proportional chamber (MWPC), and of the MCP detector that were used in the experiments. We also describe the use of a solid-state detector for precise beam energy measurements.

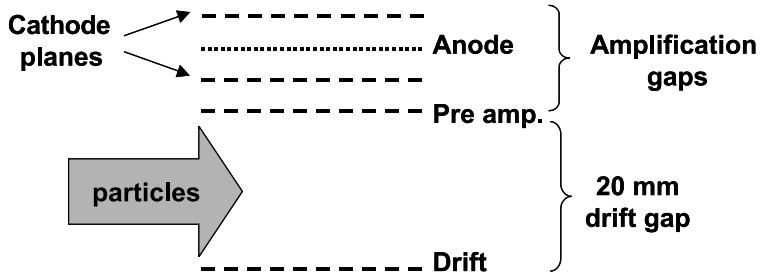

Fig. 3.6: *Schematic diagram of the MWPC detector. The anode consists of 20 μm wires with 1 mm spacing. The drift region is 20 mm wide and the amplification gaps are 6.4 mm wide.*

A low pressure MWPC

Prior to the development of our present MCP triggering system, we used a position-sensitive gaseous multiwire proportional chamber (MWPC), operated at pressure of 100 Torr; this required the use of a rather thick foil (25 μm Mylar) to separate the MWPC from the 0.9 Torr ionization volume of the ND. This MWPC was adequate for experiments with high-energy particles, but would not suit the work with low-energy protons; these particles suffer large energy degradation and scattering when passing through solid materials (foils, wires and meshes), seriously affecting the triggering system. For this reason a different MWPC, capable to work at 0.9 Torr, was designed and built; the idea was to place it immediately after the ionization volume without separating foils. A schematic description of the detector prototype is shown in figure 3.6. The detector has a 40×40 mm^2 active area, containing a drift mesh, preamplification mesh, lower cathode mesh, anode multiwire frame and upper cathode mesh. To avoid particles' interaction with the detector electrodes, the projectiles pass parallel to the electrodes, in a 20 mm drift gap; ionization electrons drift towards the preamplification gap and are further multiplied by the MWPC anode wires. The signals on the anode are then amplified by a charge amplifier followed by a timing filter amplifier.

The performance of the detector was tested with a gold-plated Am^{241} source (producing 4.25 MeV α-particles). The gaps between the amplifying electrodes and the applied voltages were carefully varied to reach optimal signals on the anodes. Example of the pulses induced on the anode are shown in figure 3.7.

This detector was found to be well suited for our application, yielding well-defined pulses at 0.9 Torr of propane and could be used as a trigger in the measurements with low energy protons. We have finally chosen another solution, the MCP mentioned before, which is capable of simultaneously providing the beam profile and serve as an efficient trigger for the DAQ.

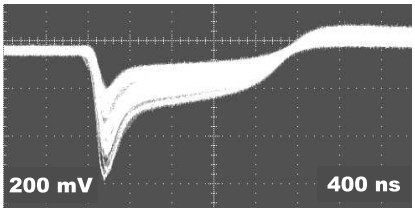

Fig. 3.7: *Signals of the MWPC anode at 0.9 Torr propane (after amplification), for the following applied voltages: V_{drift}= -330v, $V_{pre.amp}$= -230v and V_{wires}= 215v. The average pulse height is 400 mV with noise level of 50 mV.*

The MCP performance in determining beam uniformity

The MCP detector was operated at 10^{-6} Torr and was separated from the ND ionization volume by a 2.5 μm mylar window. Figure 3.8 shows a schematic diagram of the MCP detector setup; charged particles from the accelerator hit the surface of the 1st MCP and produce secondary electron emission. These electrons undergo double-stage multiplication and are accelerated onto the phosphor screen (coated by a thin layer of Al), resulting in the emission of light. The light pulses are then photographed with the CCD camera and recorded through frame-grabber card on a PC.
The great advantage of using the MCP as a triggering detector, apart from high triggering efficiency, is the valuable information it gives us about the spatial distribution of the particle-beam. It is crucial that the beam would be uniformly distributed within the set diameter, to ensure uniform exposure of the relevant biological volume in the SV.
The procedure for measuring beam uniformity was as follows: the camera was operated at a rate of 5 frames per second, each frame containing a few tens of particle-induced light spots, having various shape, size and intensities across the MCP area, due to fluctuations in the multiplication process and inhomogeneity of the phosphor screen. In order to overcome this non-uniform nature of the detector, each CCD frame was analyzed separately, marking the coordinates of the center of each light spot. Figure 3.9 shows a single frame as it looks before and after the analysis. All the analyzed frames were then added up to provide the total beam profile. About a million light spots were typically collected per operation condition, providing a statistically good estimation of beam uniformity. Figure 3.10 shows the entire broad beam 2-D image of α-particles before and after the analysis.
While the energetic α-particles produced a well-defined 20 mm diameter beam (having uniformity of more than 95%), in the case of low energy protons, we could not overcome the heavy scattering of the particles by the entrance window of the ND (separating vacuum from gas), yielding a gaussian-shaped beam, larger then the MCP detection area. Figure 3.11 shows the beam profile of the 26 MeV α-particles and the 1.03 MeV protons. We will see in chapter 4

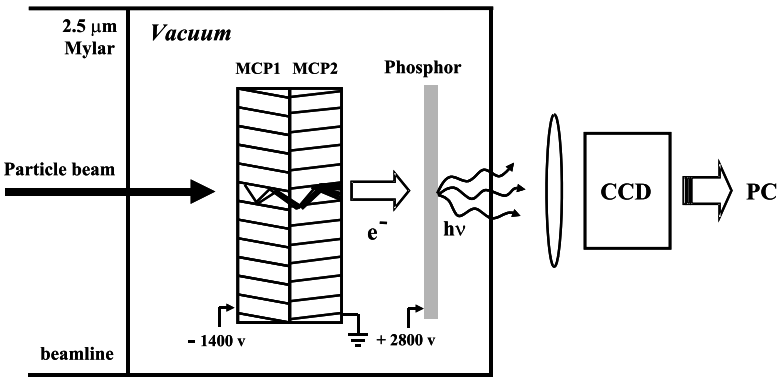

Fig. 3.8: *Schematic diagram of the MCP detector setup. The charged particles create electron avalanche in the double MCP; these electrons are accelerated onto the Al-coated phosphor screen (anode) and emit light, which is photographed by the CCD camera and recorded on a PC. The applied voltages were taken such to produce well defined pulses on the anode and strong light spots on the phosphor, easily seen by the CCD camera. The typical voltages were -1400 V on the surface of the 1st MCP, and 2800 V on the anode. The rear end of the 2nd MCP was grounded.*

that even in the case of the low energy protons, the beam may still be considered uniform for the purpose of our measurements.
Another problem arising from the fact that not all protons are detected by the MCP, is that of ion pile-up (particles that induce ions in the SV of the ND, but do not produce any trigger, so their ions could be mistakenly attributed to another particle). In order to overcome this problem, the beam flux of the protons was significantly reduced (about 800 particles per sec), to minimize the chance of pile-up events. Furthermore, by simulating the contribution of the pile-up events to the ion cluster-size distribution, based on a model of the data acquisition system, it was found that the existence of pile-up events did not distort the measurements.

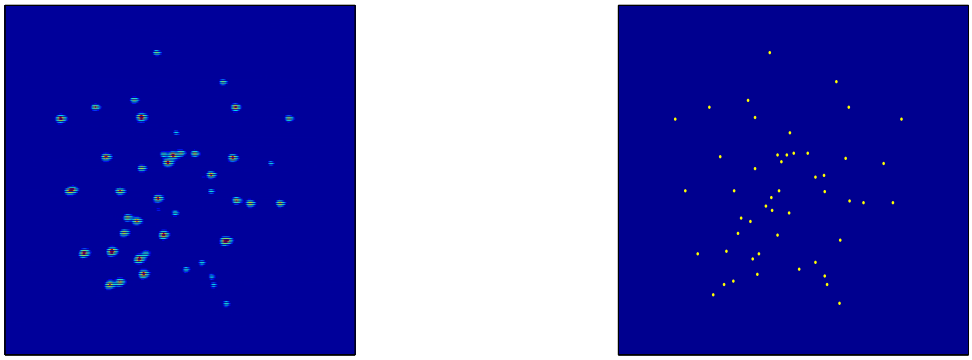

(a) (b)

Fig. 3.9: *A single frame of the illuminated phosphor taken by the CCD camera (a). Each spot represents a charged particle hitting the MCP detector. By registering the coordinates of the center of each spot, regardless of its size and intensity (b), we can overcome the non-uniformity of the detector and thus obtain an accurate spatial distribution of the detected particles.*

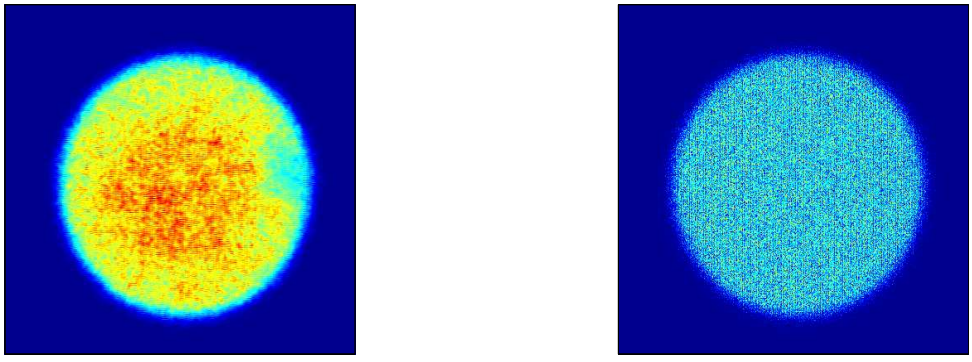

(a) (b)

Fig. 3.10: *26 MeV α-particles broad beam before (a) and after the analysis (b). Notice that the deficiency spot on the right side of the original figure completely disappears in the analyzed figure.*

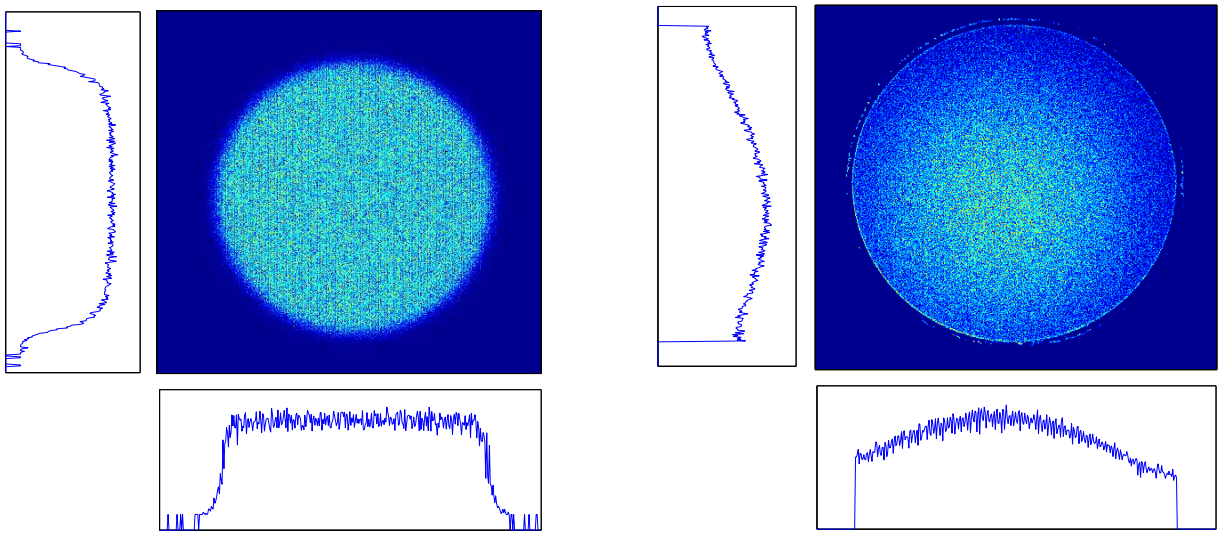

(a) α-particles (b) Protons

Fig. 3.11: *The beam projection of 26 MeV α-particles (a), and 1.03 MeV protons (b) on each axis. The α-particles produce a well defined 20 mm diameter beam, completely included in the MCP detection region of 25 mm. This beams can be considered uniform up to 5 %. The low energy protons, which are scattered by the entrance window of the ND, produce only a partially uniform beam, larger than the MCP detection region.*

Solid-state detector

A solid-state surface barrier detector allowed us to monitor the energy spectrum of the accelerator beam; this was particularly important in the measurements of low energy protons, which are subjected to large energy degradation and scattering when passing through matter.
Although simulations of the energy degradation have been conducted for choosing the appropriate scattering foils and widows thicknesses (using SRIM [32]), we preferred to conduct direct measurements of the particles energy spectra, to get a more accurate picture of the energy distribution at every stage of the beam's path (this was possible since the detector may be operated either in vacuum or in air), taking into account the inaccuracies in energy definition of the accelerator itself. In fact, at the VdG accelerator, in which the beam energy was not properly calibrated, we totaly relied on the solid state detector measurement for determining the accelerator's initial energy.
The particle-induced signals from the detector were amplified, and analyzed by a multi channel analyzer (MCA), providing the pulse height energy distributions. The absolute energy calibration of the detector was done with a spectroscopic Am^{241} radioactive source, yielding 5.49 MeV α-particles. Figure 3.12 shows the measured energy spectra of the americium source and 1.03 MeV protons (after passing through the scattering foil), and simulated energy distribution of the 26 MeV α-particles. These are the energy spectra of the particles as they enter the ND.

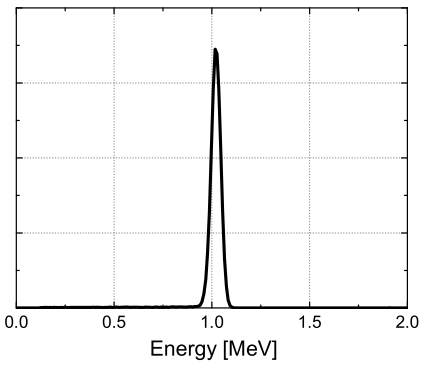

(a) Protons

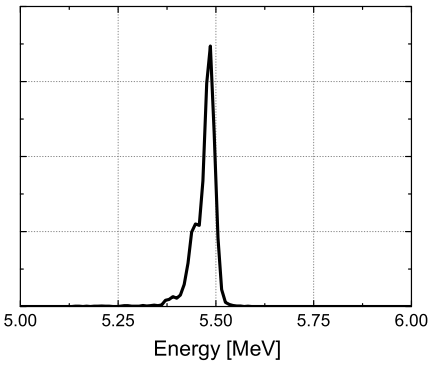

(b) Am^{241}

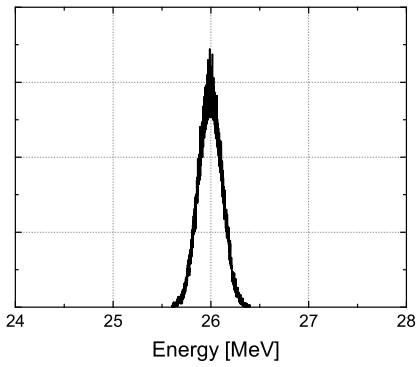

(c) α-particles

Fig. 3.12: *Measured energy spectra of 1.03 MeV protons (a), Am^{241} source, having its main peak at 5.49 MeV (b) and simulated energy spectrum of 26 MeV α-particles (c). The energies of the protons and α-particles (as they enter the ND) are: 1.03±0.03 and 26±0.125 MeV, respectively. The energy broadening $\Delta E/E$ for the protons is 6% of the mean value, while for the α-particles it is less than 1%.*

3.2 Measurement of radiation damage to DNA - Biology experiments

In parallel to the physical measurements of the ionization cluster size distributions in gaseous model of the DNA molecule, we have conducted biological measurements of radiation damage to real DNA samples, in which we irradiated plasmid DNA with equal-LET protons and α-particles (same as in the physical experiments); we measured the formation of single- and double-strand breaks as well as DNA inactivation, following the irradiation at different doses. The irradiated plasmids were analyzed for the formation of strand breaks using gel electrophoresis [33], and for general clustered damage (several strand breaks and/or base damages in close proximity) by a bacterial transformation assay. The details of these experiments are summarized below.

3.2.1 Irradiation setup

The setup used for the biological experiments is shown in figure 3.13. This setup was mounted on the accelerator beamline directly following the ND (the beam size-control collimator was removed to obtain a beam diameter larger than 20 mm). As before, the beam was scattered by a thin metallic foil placed 3 m upstream from the irradiation chamber, to ensure uniform irradiation of the entire sample. After exiting the beamline through a 12.7 μm-thick Kapton window, 2.5 cm in diameter, the particles beam passes through an air gap ionization chamber (composed of two aluminized Mylar foils, allowing to monitor the absorbed dose and dose rate) and reaches the DNA sample.
A droplet (5 μl in the case of α-particles irradiation, and 3 μl in the case of protons irradiation, see below) of plasmid solution in phosphate buffer was placed on a 20 mm diameter quartz disk, and pressed down by a 12.7 μm Teflon foil (forming a 20 mm diameter and 16 μm or 10 μm thick solution film, respectively). The sample holder contained a reservoir of the irradiation buffer (in order to prevent sample evaporation), and sealed with an O-ring; this allowed irradiation of up to 10 hours without noticeable evaporation of the sample.

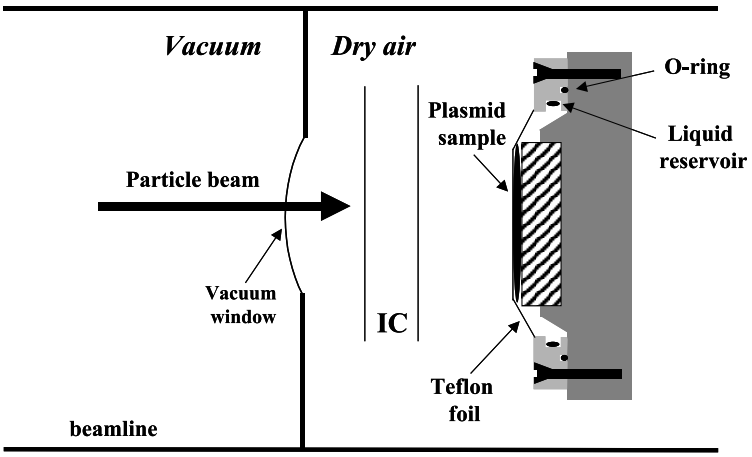

Fig. 3.13: *Irradiation setup for the biology experiments. See text.*

3.2.2 The plasmid solution

The DNA target used for these experiments is the pHaze plasmid, described in [34]. It contains a gene for antibiotics (Ampicillin) resistance and several other genes required for replication in E.Coli bacteria. The plasmids were placed in a phosphate buffer containing 2 or 200 millimolar (mM) of the radical scavenger glycerol; the scavenger concentration affects the mean free path (MFP) of the radicals in the solution. At 2 mM concentration, the MFP of the radicals is relatively large (up to 80 nm), with life time of 10^{-7} sec [12], allowing the radicals to diffuse a large distance (compared to the DNA size) before they collide with other molecules. At scavenger concentration of 200 mM (corresponding to real cellular conditions), we expect to find a dependence of the damage on the "clustering" of the ionizations, since the radicals (having a lifetime of only 10^{-9} sec) recombine only a few nm ($\sim$8) from where they were formed, thus correlating the radiation energy deposition patterns with the induced damage on the DNA molecules.

3.2.3 Energy degradation through the sample

The irradiation of the DNA samples require the particles to pass through several foils before entering the sample, causing their energy spectrum to degrade and broaden. Moreover, the sample thickness itself causes large energy straggling, resulting in energetically non-uniform irradiation of the plasmids. This effect becomes crucial in the case of low energy protons, which could loose more than a third of their energy throughout the sample. When comparing the biological effectiveness of equal-LET particles, we must minimize the energy variations within the sample, so the plasmids would be exposed to as uniform LET radiation as possible. Therefore, it is extremely important to reduce the sample thickness (providing that enough substance can be extracted from the sample holder after irradiation, for the analysis). For the 26 MeV α-particles irradiation, we used a relatively thick (but easy to handle) sample of 16 μm, since the energy degradation of the α-particles throughout the sample was only 2%. In the case of 1.03 MeV protons, a thinner sample of 10 μm was used, resulting in overall energy variation of 15% from one side of the sample to the other. Figure 3.14 shows the calculated variation in LET of the α-particles and protons as they pass through the plasmid sample, due to energy degradation.

3.2.4 DNA damage analysis

Plasmid DNA is a good model system for the study of single- and double-strand breaks, since the plasmid changes its shape according to the induced damage type; the undamaged plasmid is a closed supercoiled (SC) ring of DNA, containing about 10^3 base-pairs. The occurrence of isolated single-strand breaks (SSB) causes the plasmid to uncoil, forming a relaxed ring (open circle). Induction of a double-strand break (DSB) will cause the plasmid to linearize. These three states, due to their different mobility, can be distinguished quite clearly by standard gel electrophoresis; the irradiated plasmids are loaded onto the agarose gel, drifted under an electric field (1 V/cm, for 18-20 hours), and stained by a fluorescent marker (Ethidium Bromide). The supercoiled (undamaged), relaxed (SSB damage) and linear plasmids (DSB damage) appear as distinct bands on the gel (see figure 3.15).

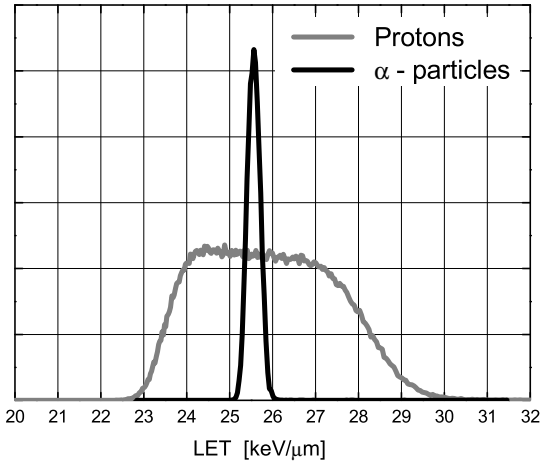

Fig. 3.14: *LET spectrum of 26 MeV α-particles and 1.03 MeV protons as they pass through the plasmid sample of width 16 μm and 10 μm, respectively. The initial energy of the particles was taken such that the LET at the middle of the sample would be 25.5 keV/μm. The variance in the α-particles LET is $\pm$1%, while the protons LET changes by $\pm$ 7.5% from its mean value.*

The fraction of plasmids on each band is compared to a statistical model developed by Cowan [35]; from a fit to these predictions, we can obtain μ, the average number of SSB per plasmid per krad, and ϕ, the average number of DSB per plasmid per krad. The measurement error in μ and ϕ was evaluated by repeating the experiment several times and calculating the standard deviation.
The determination of gene inactivation is done by a bacterial transformation assay, since gene inactivation (irreparable damage) due to clustered damage that contains multiple base damages (BD), cannot be detected by gel electrophoresis. In this assay, the irradiated plasmids are used to transform E.Coli bacteria to antibiotics resistant; when placed under stress (strong temperature variations), the bacteria incorporates the plasmid DNA in its vicinity into its own genome. The bacteria are then grown on an antibiotic medium and only bacteria which have successfully incorporated an intact plasmid, or a plasmid having an isolated (reparable) damage (either one SSB or one BD), will survive.
Using the Cowan model, replacing the strand breaks parameters by parameters related to base damage, we can also predict the fraction of inactivated plasmids. These new values are denoted μ' - the number of isolated damages per plasmid per krad, and ϕ' - the number of complex damages per plasmid per krad. The main difference between this assay and the previous one is that it is sensitive also to base damages and therefore we expect larger values for μ' and ϕ' obtained from a fit to this model [36]. An example of the analysis for plasmids irradiated by 26 MeV α-particles is shown in figure 3.16.

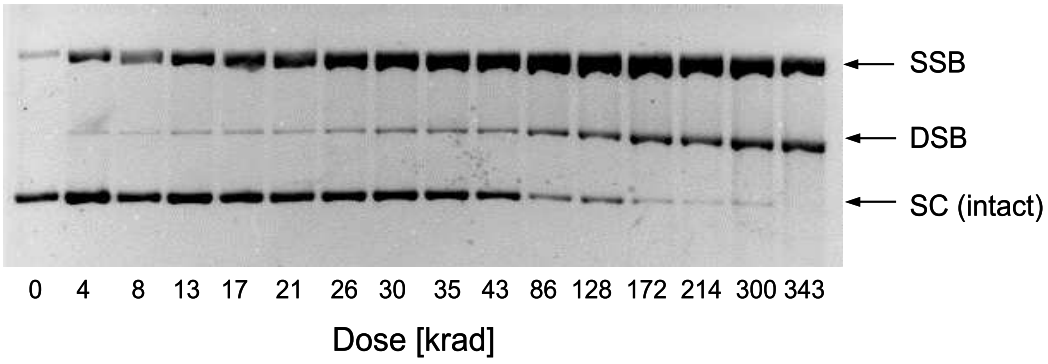

Fig. 3.15: *Gel electrophoresis of pHaze plasmids at a scavenger concentration of 200 mM, irradiated by 26 MeV α-particles at different doses. The amount of undamaged supercoiled plasmids (SC) decrease with dose, while the amount of plasmids having double-strand breaks (DSB) increases. The number of plasmids having single-strand breaks (SSB) increases at start, up to the level (about 200 krad) when accumulative processes begin to convert SSBs into DSBs, resulting in the decrease of the number of SSBs.*

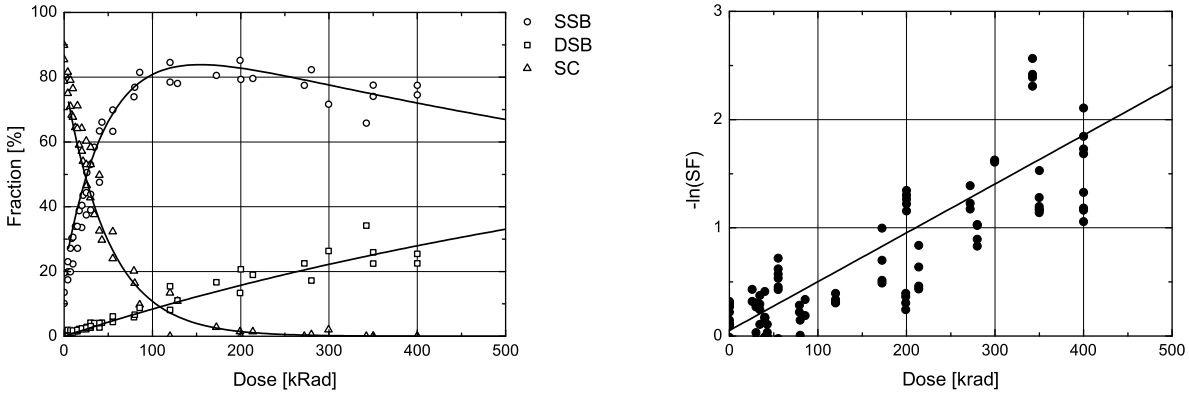

(a) Gel electrophoresis

(b) Bacterial transformation

Fig. 3.16: *DNA damage analysis followed by 26 MeV α-particles irradiation (data from 3 independent experiments). (a) Gel electrophoresis assay: the graph presents the fraction of each type of plasmid shape as a function of absorbed dose. The isolated symbols represent the SSBs, DSBs and supercoiled (SC) plasmids. The lines show the model fit to the experimental results. (b) The bacterial transformation assay gives the average number of inactivation events per plasmid (assuming poisson distribution of the induced damages), showing linear behavior of complex damage as a function of dose (SF is the surviving fraction of bacteria, containing intact plasmid).*

4. Monte Carlo simulations

In order to prepare the experimental work and gain understanding of the ionization processes and resulting cluster size spectra measured by the ND, we have implemented a detailed particle interaction model and a Monte Carlo (MC) simulation code. It has been developed in cooperation with Dr. B. Grosswendt, a world-expert in the field of interaction of radiation with matter, from PTB-Braunschweig, Germany.
The MC simulation uses measured and model-calculated interaction cross-sections of α-particles, protons and electrons in propane [31] (including the specific case of K-shell ionizations, see section 4.3). The code calculates the ionization track structure in the gas, for any given type of radiation. The secondary electrons induced by the primary particles are followed through the gas until their energy reaches a value below the ionization threshold (11 eV); an example of a simulated fraction of a charged-particle track with δ-electrons is shown in figure 2.2 on page 5. In addition, the calculated ion extraction efficiency map (see fig. 3.2) is applied to the simulation, to obtain full correspondence to the ND experimental system. A detailed description of the simulation procedure is given in appendix A of [26].
The MC simulation is an extremely important tool, which helps us to calculate the expected ion cluster size distributions in a variety of experimental conditions such as gas pressure, beam radius, particle location with respect to the SV, electric field, etc. and to learn about the characteristics of the track structure for each radiation type.
In this chapter I will discuss several topics in which the simulations contributed a great deal to our understanding of the experimental results and their interpretation, and helped us in the decision-making process regarding the selection of appropriate experimental conditions.

4.1 Range of δ-electrons: determination of beam radius

One of the problems we encountered in the planning of the physical experiments was determining the necessary beam diameter that would yield uniform irradiation of the relevant biological-like volume in the ND, assuring no spatial correlation between the target volume and the radiation trajectories, as in the real biological case. To achieve this, the beam radius must be larger than the size of the target volume by R_δ - the maximal range of δ-electrons in 0.9 Torr propane (a larger beam would only give additional "zero" clusters to the ion cluster size distribution, since no extra ionizations would reach the target volume).
The δ-electrons maximal kinematically-allowed range in 0.9 Torr propane is 15 m!, yet only a small fraction of the δ-electrons actually realize this limit, therefore it is not wise to describe it as the δ-electrons range in our experiment. Instead, we use the MC simulation code to set an "effective range", which will include most of the δ-electrons, but at the same time be

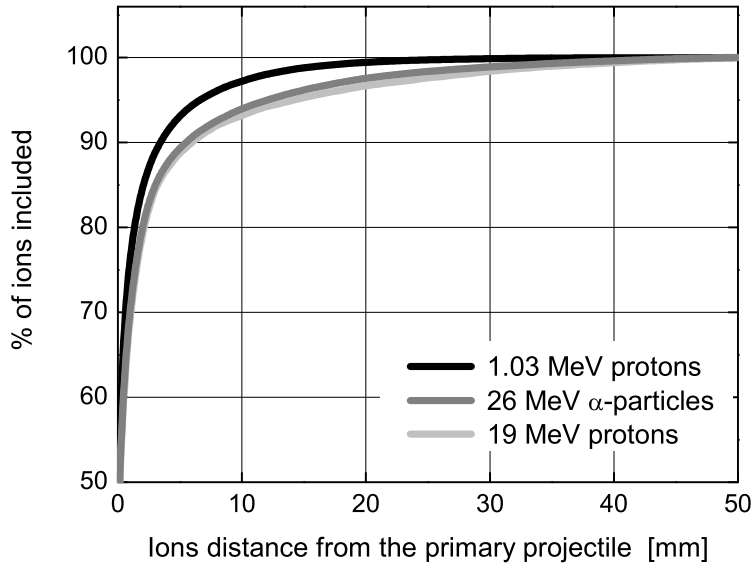

Fig. 4.1: *The cumulative fraction of the ions as a function of distance from the primary projectile. The low energy protons have smaller δ-electron range, compared to the equal-LET α-particles and high energy protons. According to the graph, if we irradiate the SV with a 20 mm diameter beam, we can expect uniform irradiation of the biological relevant volume of up to 94% (in average) in the case of high energy protons and α-particles, and up to 97% in the case of low energy protons.*

experimentally-realistic.

The method used to monitor the δ-electrons range is simulating a narrow beam (0.5 μm radius) passing through an infinitely large SV with unit ion collection efficiency, and look at the coordinates where the ions were created lateral to the beam direction. By this approach we can learn about the fraction of the ions induced as a function of distance from the primary projectile, and thus extract the effective range of the δ-electrons in our experiment. Figure 4.1 shows the cumulative fraction of the ions as a function of distance from the primary projectile, for high-energy protons and for equal-LET protons and α-particles.

The analysis of the ions spatial distribution shows one of the most interesting and meaningful features of equal-LET protons and α-particles; the low energy protons induce more ions closer to the primary-particle's path than the α-particles. This trend can be explained since the low energy protons (1.03 MeV) are slower than the high energy (26 MeV) α-particles, therefore they induce less energetic δ-electrons, which have smaller range; this causes the ions to be confined in a smaller area around the primary projectile.

When translating this result into the biological relevance of the radiation, we may conclude that the ions induced by the protons are more clustered; therefore they are expected to cause complex damages which are harder for the cell to repair. **This should make the protons more lethal than equal-LET α-particles**, which is indeed the trend seen in the biological experiments conducted by us (see section 5.2).

4.2 Equivalence of the SV to the DNA molecule

The rational of choosing the current configuration of the SV is its equivalence to a segment of the DNA double helix and it surrounding water layer. The acceptable relevant size for the study of radiation effects on DNA is a 16 nm long cylinder with diameter of 4 nm, corresponding to a 50 base-pair DNA molecule surrounded by water [21, 22]. According to the theory of modelling in gas, the equivalent volume in our current experimental conditions should be a 7.6 mm long cylinder with diameter of 1.9 mm.
The total SV has a cylindrical shape of height 50 mm and diameter of 3.2 mm, with a varying ion collection efficiency (see figure 3.2). This volume can be cut into segments in the vertical direction, by applying the time-cut selection tool in the off-line analysis of the ions arrival times (see section 3.1.1 of the DAQ system and analysis), selecting only the ions induced in a desired length of the SV. In the horizontal direction, however, we have no control over the diameter of the collection area, which is solely defined by the zero collection efficiency limits. Therefore, the experimentally available biologically-relevant volume has a diameter that exceeds the desired model diameter by 30%, and has an efficiency gradient from the center towards its edges.
In order to examine the equivalence of the experimental biologically-relevant volume to the desired model volume with diameter of 1.9 mm, we have created special ion collection efficiency map, representing different regions of the SV, and introduced them into the MC simulation code, thus producing the ion cluster size distribution in each region. Figure 4.2 shows the maps representing the 3 regions of interest: the time-cut map (green), representing the biologically-relevant volume available in the experiment, and its division into two parts: the inner shell of 1.9 mm diameter (red), and the outer shell (blue).
When comparing the ion cluster size distributions (normalized without the "zero" clusters, which have no biological significance) from the 3 regions (figure 4.3), we can see that the distribution of ions in the time-cut region and the inner shell are very similar to each other, meaning that the ions created in the outer shell do not significantly change the ionization patterns in the time-cut region. We can thus establish the equivalence of the experimental biologically-relevant volume to the desired DNA model.

4.3 Comparison between protons and α-particles of equal LET

The motivation to conduct nanodosimetric measurements of equal-LET protons and α-particles was based on the difference predicted by the MC simulation in the ion cluster size distributions, showing that protons have higher probability to produce large clusters of ions than α-particles. In the course of this project, the simulations have been thoroughly improved, taking into account more complex physical phenomena occurring in the ionization process.
The latest simulation version includes the additional process of Auger electrons, or K-shell ionization; in the ionization process, there exists a probability of ionizing an inner shell of the propane molecule atoms, creating a vacancy in the core, which is filled by electrons from higher levels. The energy liberated in this process is transferred to a second electron, called the Auger electron, which carries enough energy to leave the atom, creating a doubly-ionized molecular ion. This process may influence the ion cluster size distribution in two ways; the Auger electron acts like a δ-electron, and induces about 10 more independent ionizations in the

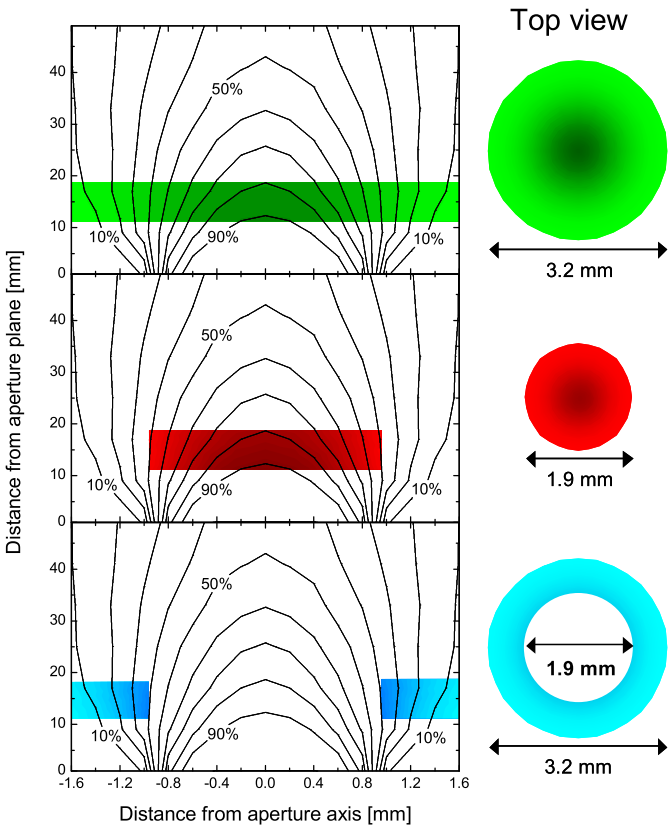

Fig. 4.2: *Special ion collection efficiency maps used to investigate the validity of the experimental results. The time-cut map (green) represents the experimentally measured biologically-relevant volume. This map is divided into the inner shell (red) and outer shell (blue). The maps are introduced into the MC simulation code, which produces the ion cluster size distribution in each region.*

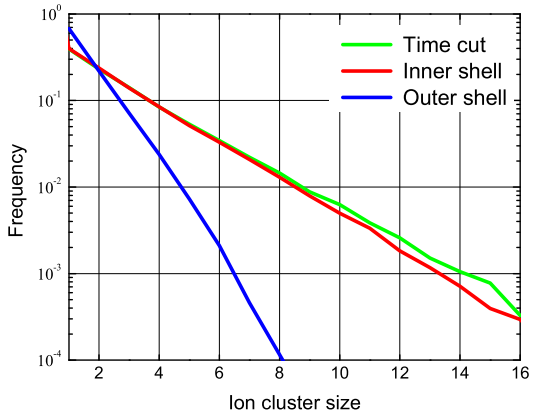

Fig. 4.3: *Simulated ion cluster size distributions (non zero analysis) produced in each region. The ion created in the outer shell (blue) contribute only a small fraction to the time-cut cluster size distribution (green), making it possible to consider the time-cut region as having the correct diameter of 1.9 mm (red), as required according to the theory of modelling in gas.*

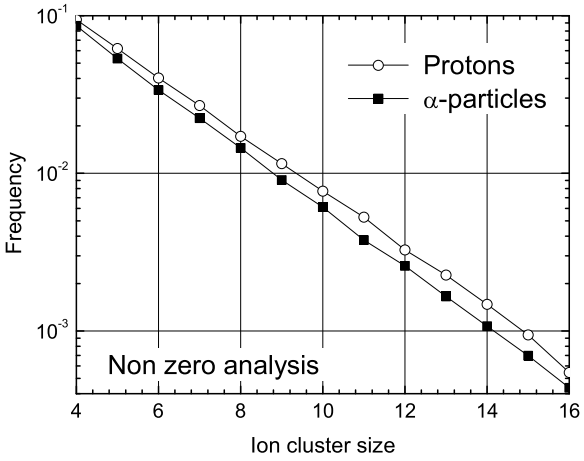

Fig. 4.4: *Simulated ion cluster size distributions of 1.03 MeV protons and 26 MeV α-particles, with beam diameter of 20 mm (non zero analysis). The protons show 20% higher probability to induce ion clusters of a given size.*

gas. In addition, the doubly-charged molecular ion from which it originated, carries enough potential energy to produce two singly-charged ions. Thus each K-shell ionization adds a total of 12 ions to the overall number of ions induced in the gas.
Since K-shell ionization cross-sections do not exist for molecules, we considered the cross-section for carbon atoms, which constitute the propane gas used in our experiment. In the case of the high energy protons and α-particles, the cross-sections are calculated by a model described in [37]. At low energies (like 1.03 MeV protons), however, this model does not hold, and the cross-sections are taken from well-recognized experimental data [38]. Figure 4.4 shows simulated ion cluster size distributions of 1.03 MeV protons and 26 MeV α-particles (non zero analysis).

4.3.1 The differences in track structure

We wanted to check to what extent the differences in the ion cluster size distributions induced by the equal-LET protons and α-particles depend on their different δ-electrons range (as discussed in section 4.1).
The primary-ionization cross-section of protons ($4.06 \cdot 10^{-16}$) is larger by 10% from that of the α-particles ($3.69 \cdot 10^{-16}$). The reason for this is that the δ-electrons produced by the α-particles are more energetic, and induce more secondary-ionizations. Since the total amount of energy-loss (on macroscopic scales) is the same for both particles, the α-particles would produce less primary-ionizations. According to the simulations, protons' primary-ionizations are responsible for 49% of the overall ionizations, while α-particles' primary-ionizations induce only 45% of the ions. However, we must keep in mind that the secondary-ionizations of the α-particles are less dense, therefore when examined on nanometric scales, they appear to be less frequent.
In the simulation, we "turned off" the creation of the δ-electrons and looked at the ion cluster size distributions of the particles, with or without the contribution of the δ-electrons (figure 4.5).

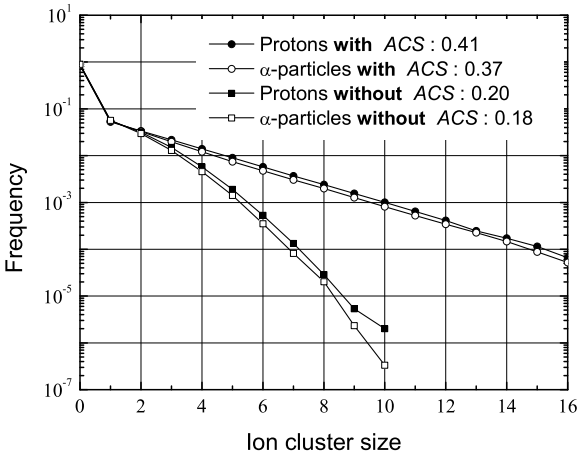

Fig. 4.5: *Simulated ion cluster size distribution of 1.03 MeV protons and 26 MeV α-particles, with and without the contribution of δ-electrons. We can see that the δ-electrons are responsible for the production of large clusters (10 and up). The graph shows that the differences in the track structure exist also in the primary-ionizations patterns, which are denser in the case of the protons, due to the different energies of δ-electrons emitted by the particles (see text).*

The difference between the average ion cluster size (ACS) of the protons and α-particles remains 10%, with or without the δ-electrons. The graph also shows that δ-electrons are responsible for the induction of the large ion clusters, which are more biologically hazardous.
This example shows that the differences in the track structure of equal-LET protons and α-particles is present in both the primary and secondary ionization patterns on nanometric scales, having higher densities in the case of the low-energy protons.

4.4 Verification of low energy protons experimental results

The measurements with low energy protons were not preformed under ideal conditions due to the energy straggling and scattering of the particles as they passed through the ND. Thus, the experimental results had to be confirmed to arise from real physical phenomena and not originate from experimental artifacts.
The first drawback was the rather broad energy spectrum of the particles reaching the ND (about 6% broadening, see figure 3.12), and the second imperfection was a non-uniform beam profile, measured by the MCP detector. Since we could not overcome these effects experimentally, we had to use the simulations to verify our results, so we will be able to compare them to the results of the α-particles experiments, which did not carry such deformities in the beam quality, but had a rather narrow energy spectrum (less than 1% broadening), and a well-defined uniform beam of 20 mm diameter.
In order to do so, The energy spectrum and beam profile of the protons, as measured in the experiment, were introduced into the MC simulation code, and compared to the ideal situation of spatially uniform, monoenergetic, 20 mm diameter beam. The simulated ion cluster size

distributions in both cases are given in figure 4.6.
From the total analysis (including "zero" clusters), we get a discrepancy between the distributions, originating from the fact that the protons' experimental beam, larger than the 20 mm ideal beam, induces more "empty" clusters in the SV and therefore changed the normalization of the distribution (the total probability is normalized to 1). Yet, when comparing the non-zero clusters distribution, which is relevant for estimating the biological effects of the radiation, we see no discrepancy between the two beams.
Although the simulation results and the measured experimental results do not coincide completely, we believe that if the simulations predict no difference in the distributions, the experimental results should behave in the same manner, therefore we can assume that the measured ion cluster size distribution of low energy protons were not much effected by the quality of the beam.

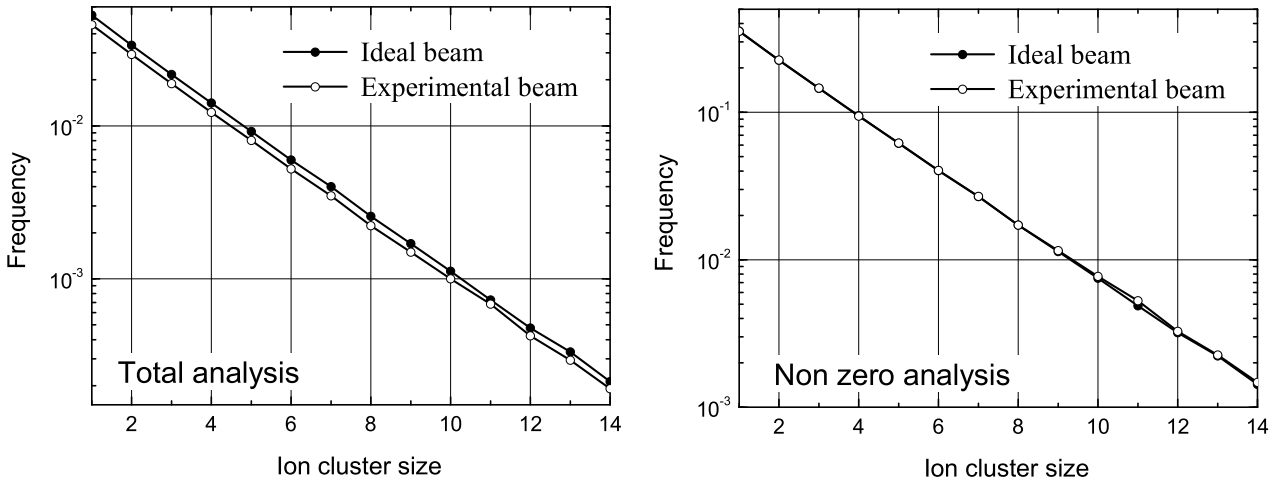

(a) (b)

Fig. 4.6: *Simulated ion cluster size distributions of 1.03 MeV protons in the ideal case (20 mm diameter, monoenergetic and spatially uniform beam) and as existed during the measurements at the accelerator (broad energy spectrum, spatially non-uniform beam, with diameter larger than 20 mm). figure (a) shows the total cluster size analysis, while figure (b) gives the non-zero cluster analysis, where the two distributions coincide.*

5. Scientific results and discussion

5.1 Physics results

We have preformed nanodosimetric measurements of 1.03 MeV protons and 26 MeV α-particles, having equal-LET value of 25.5 keV/μm. The measurements of the α-particles were done with a uniform beam of diameters 6.5 and 20 mm, while the protons, due to scattering in the ND entrance window, had a gaussian beam profile with FWHM of 24 mm (at the SV). It should be reminded that MC simulations have shown that the gaussian shape of the beam does not affect the ion cluster-size distribution (see section 4.4).

5.1.1 Effect of beam diameter

The cluster size distributions of the α-particles with beam diameters of 6.5 mm and 20 mm are shown in figure 5.1. Comparing the two distributions, we see that the beam diameter influences only the frequency of "zero" clusters (the broader beam induces more "empty" clusters in the SV). However, when normalizing the distributions without the "zero" clusters (figure 5.1.b), the distributions overlap. These results indicate that within the current resolution of our experimental system, a beam diameter of 20 mm is broad enough to be considered as "infinite" relative to the SV size.

Another interesting feature of different beam diameters is their respective ion arrival time distributions, shown in figure 5.2; these distributions indicate the ions locations along the SV, with respect to the extraction aperture. We see that the 6.5 mm beam ion arrival time distribution is narrower than that of the 20 mm beam. Both distributions are flat, indicating that the beams were spatially uniform.

From the information given above, we conclude that even though the ions induced by the two beam diameters are spread over a different region in the SV, they induce similar cluster size distributions (not including the "empty" clusters). This result may be explained by the size and shape of the SV and its efficiency gradient; the SV is a 50 mm high cylinder, with diameter of 3.2 mm (see figure 3.2). The efficiency in the vertical direction (along the SV axis) changes by approximately 12% over 10 mm, while the efficiency parallel to the extraction aperture, 15 mm above it, drops from 85% to zero in just 1.5 mm from the SV axis. This means that even though we irradiate the SV with different beam diameters, the vertical difference in the ion efficiency collection is negligible, while in the horizontal direction, since the SV is very narrow, enlarging the beam diameter would only increase the number of empty clusters in the distribution. Therefore, the ions induction per projectile remains identical in both cases.

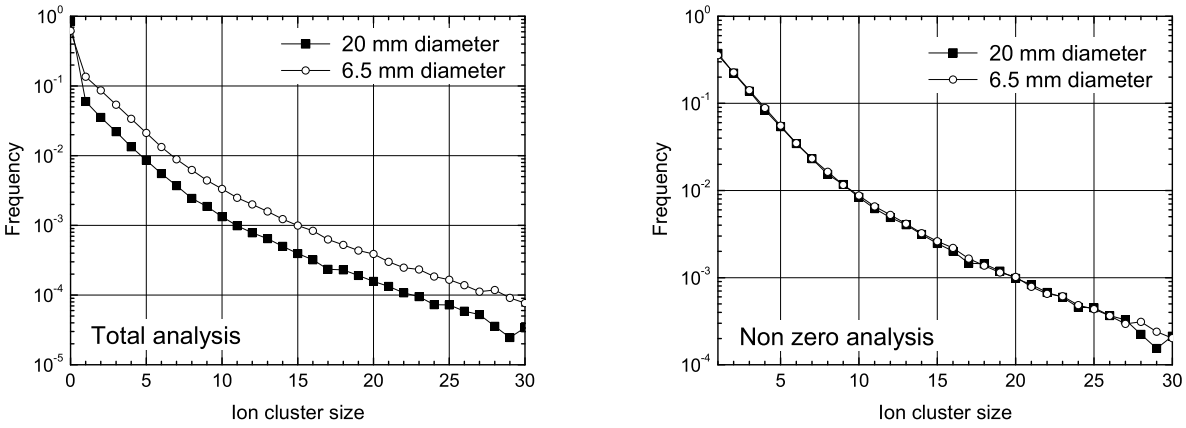

(a) (b)

Fig. 5.1: *Measured ion cluster size distributions of 26 MeV α-particles with beam diameters of 6.5 and 20 mm. Figure (a) shows the total cluster analysis, while figure (b) gives only the non zero clusters analysis. We see that the two beams differ only in the number of "empty" clusters they induce, therefore irradiation of the SV with a 20 mm beam can be considered as uniform irradiation.*

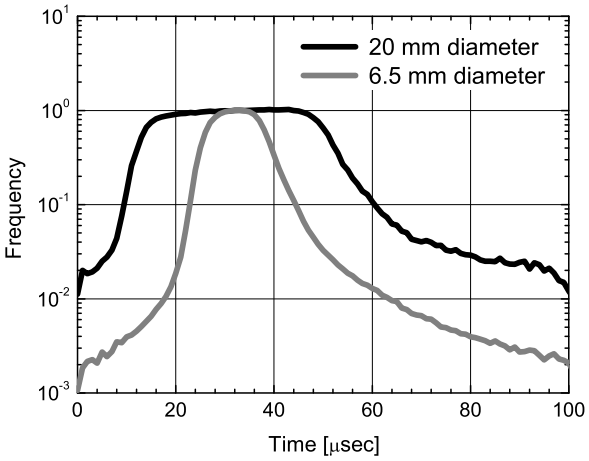

Fig. 5.2: *Distribution of the ion arrival time of 26 MeV α-particles with beam diameter of 6.5 and 20 mm. The arrival time of the ions is equivalent to their distance above the extraction aperture, so as expected, the 6.5 mm beam induces ions in a smaller region, equivalent to about 8 mm, around the center of the SV.*

5.1.2 The biologically-relevant volume

In order to isolate the cluster size distribution in the biologically-relevant volume, we have selected (off-line) ions induced in a segment of the SV. This was done by applying a time-cut selection tool; for each projectile, we have counted only the ions arriving between 22 and 41 μs (i.e. ions that were induced in the 7.6 mm long biologically-relevant volume). Figure 5.3 shows the arrival time distribution of 1.03 MeV protons and 26 MeV α-particles with beam diameter of 20 mm (or somewhat larger in the case of the protons). The highlighted black section shows the time-cut region, selected out of the whole distribution. We can see that while the distribution in the case of the α-particles is completely flat, indicating that the biologically-relevant volume was exposed to a uniform irradiation field, the protons distribution suffers a small (but non-significant) curvature, since the beam was not spatially uniform, due to particle scattering.
Figure 5.4 shows the cluster size distributions of 26 MeV α-particles from the whole SV and from the biologically relevant volume (the protons' distribution has a similar trend). We see that the time-cut selection reduces the cluster size and adds more "empty" clusters, so the distribution is shifted left and down (due to normalization of the probabilities) with respect to the total SV data.

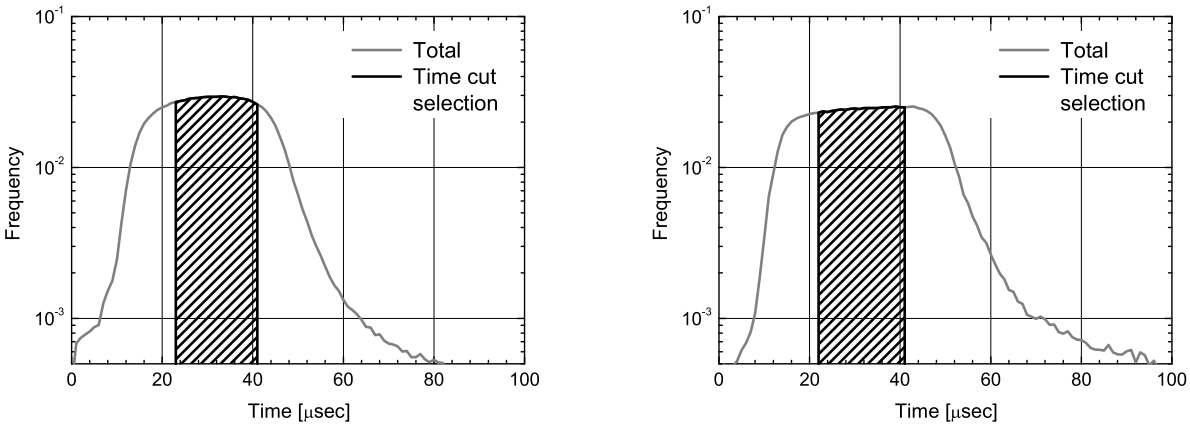

(a) Protons (b) α-particles

Fig. 5.3: *Ion arrival time distributions of 1.03 MeV protons (a) and 26 MeV α-particles (b). The highlighted sections represent the time-cut selected regions, defining the 7.6 mm (16 nm) biologically-relevant volume.*

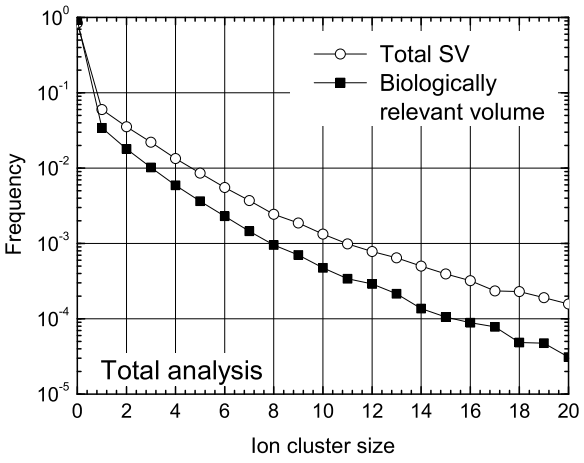

Fig. 5.4: *Comparison between measured ion cluster size distributions of 26 MeV α-particles, collected from the whole SV and from the biologically-relevant volume (selected by the time-cut analysis). The latter is reduced compared to the total SV distribution, since the ion clusters are smaller and there are more "empty" clusters.*

5.1.3 Comparison of equal-LET protons and α-particles

Figure 5.5 presents the measured and simulated ion cluster size distributions of 1.03 MeV protons and 26 MeV α-particles, in the total SV (figure 5.5.a) and in the biologically-relevant volume (figure 5.5.b). The simulated distributions are in rather good agreement with the experimental results (up to the order of 10^{-2}). The enhanced tails in the experimental data at lower frequencies, are probably due to instrumental systematic ion "over-counting", observed before [26] and yet unexplained.
The graph shows that the protons have ∼20% higher probability to produce ion clusters of a given size than the α-particles. This difference arises from the fact that the track structure of the protons is denser (see sections 4.1 and 4.3.1). Since the protons induce more confined ion clusters, their chance to be created in the SV is larger, thus we see higher frequencies in the cluster size distribution. This trend of the protons ability to induce more clustered ionizations was also seen in the biological experiments (see below), and was previously observed in survival studies of irradiated cells [5].

5.2 Biological results

We have preformed plasmid DNA irradiation with equal LET protons and α-particles, at scavenger concentrations of 2 mM and 200 mM. In order to minimize statistical errors, the α-particles irradiations were repeated 3 times. The protons irradiation was done so far only once and will be repeated in the near future.
The classification of the damage caused by the radiation was done by a gel electrophoresis assay, which determined the amount of single-strand breaks (SSB) and double-strand breaks (DSB)

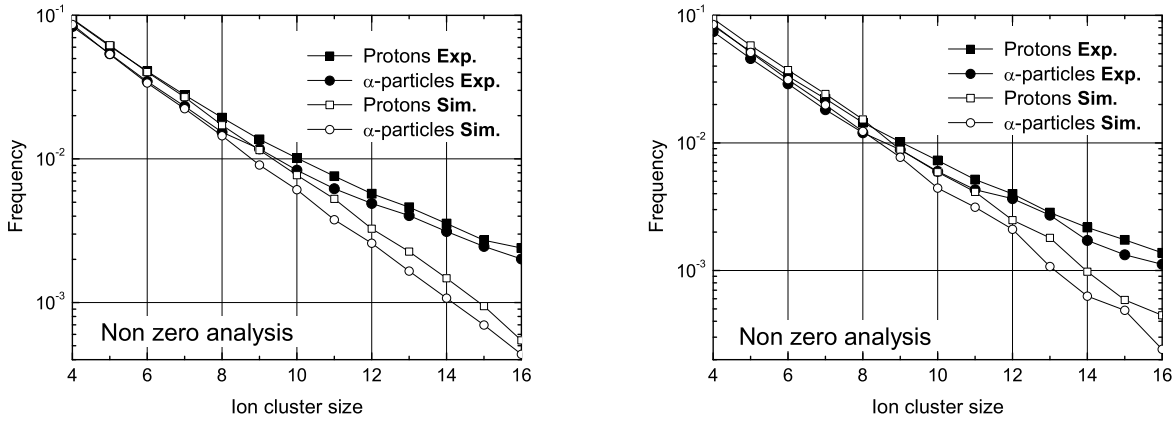

(a) Total SV

(b) Biological relevant volume

Fig. 5.5: *Measured and simulated ion cluster size distributions of equal-LET protons and α-particles, in the total SV (a), and in the biological relevant volume (b). The protons have about 20% higher probability to induce ion clusters of a given size, compared to the α-particles.*

in the irradiated plasmids, and by a bacteria transformation assay, which is also sensitive to base-damages (BD), and measures gene inactivation, i.e. the amount of clustered irreparable damage caused to the plasmids (see section 3.2.4).
The experimental data was fitted to a statistical model developed by Cowan [35], from which the following parameters are extracted: μ - the number of SSBs per plasmid per krad, ϕ - the number of DSBs per plasmid per krad, μ' - the number of isolated damages per plasmid per krad (BD or SSB), and ϕ' - the number of complex damages per plasmid per krad.
The following table presents the results for the two types of radiations (the parameters that obtained negative or very close to zero values were ignored). Since the proton irradiation was done only once, there are no statistical errors attributed to its results.
By comparing the values obtained for the protons and α-particles, we see that in both scavenger concentrations, we have almost twice as much DSBs per plasmid per krad (ϕ) for the proton irradiation, while the amount of SSBs (μ) tends to have smaller variations. At high scavenger

Projectile	Scavenger concentration	μ	ϕ	μ'	ϕ'	μ'/μ	ϕ'/ϕ
1.03 MeV	2 mM	0.126	0.013	-	0.042	-	3.1
Protons	200 mM	0.029	0.002	0.117	0.0054	3.9	2.7
26 MeV	2 mM	0.116±0.04	0.008±0.002	0.54	0.029±0.007	4.6±1.6	3.7±1.3
α-particles	200 mM	0.019±0.004	0.0009±0.0002	0.15±0.08	0.003±0.001	7.9±4.5	3.8±1.5

Tab. 5.1: *Summary of the biology measurements data. μ and ϕ represent the number of SSBs and DSBs per plasmid per krad, respectively. μ' is the number of isolated damages per plasmid per krad (base damages or strand breaks), and ϕ' - the number of complex damages per plasmid per krad.*

concentration all damage yields are about 10 times smaller, as expected from the reduced range of the free radicals.
The ratio μ'/μ provides the contribution of base damages to the amount of isolated damages. From the literature [36], we expect μ'/μ=3.5 for low-LET particles (there are no published experimental studies on the LET-dependence of this ratio, although simulations indicate that it should not be LET-dependant). From the data we see that μ' is indeed 3-5 times larger than μ, except for the α-particles at high scavenger concentration, for which we get a value of 7.9, but with a large statistical error.
The ratio of ϕ'/ϕ reflects the increase in clustering of the biological damage; the smaller the ratio, the higher probability that the irreparable damage originated from a DSB. This indicates that the protons, having smaller ϕ'/ϕ compared to the α-particles, induced more clustered damage, as expected.
Although similar trend was observed by Goodhead *et al.* (1992), who used irradiated cells survival-curves to compared the biological effectiveness of protons and α-particles with LET values between 20-23 keV/μm, our results, which are based on the direct analysis of DNA molecules, hold more basic and fundamental information about the difference in the biological effectiveness of the particles, and its origin.
From these results, showing that protons have higher biological effectiveness than equal-LET α-particles, we can conclude that there is a clear correlation between the track structure of the radiation field on the biological end effect, meaning that the DNA is very much sensitive to the spatial correlations between ionizations on nanometric scales.

6. Conclusions

In this work we have conducted a direct comparison between physical and biological effects of equal-LET protons and α-particles, by measuring both the ionization patterns of the particles on DNA-equivalent nanometer scales, and the biological effectiveness on real DNA samples.

The major part of this work was devoted to the preparation of both experiments, to make sure that they will be done under precise and identical conditions for both particles, in order to be able to compare the differences between their effects.

The physical measurements were done using a novel nanodosimetric experimental system, in which we created an expanded model of the DNA molecule; it permitted accurate measurements of the ion cluster size distribution for each radiation type, in a tissue-equivalent gas volume of biologically-significant size.

The physical experiments have been conducted under conditions dictated by the biological irradiation conditions. For that purpose the following steps were taken:

1. The irradiation was done with a broad particle beam of diameter 20 mm, to avoid any spatial correlations between the particles' trajectories and the target volume. We have verified (both experimentally and by simulations) that the chosen beam diameter is broad enough to be considered "infinite" within our experimental resolution.

2. The beam's spatial uniformity was verified by measuring its profile with a dedicated MCP detector coupled to a CCD camera. The beam was found to have no more than 5% variations in the case of the α-particles. The proton beam, due to large scattering from the entrance widow of the nanodosimeter, had a gaussian shape, with about 30% variation in the beam profile. However, the MC simulations, developed within the work, have shown that this variation did not effect the experimental results significantly, meaning that the proton beam yielded practically the same ion cluster size distribution as if it was uniform.

3. The energy spectrum of the protons and α-particles beams (measured by a solid-state detector) was found to be 1.03 MeV $\pm$3% and 26 MeV $\pm$0.5%, respectively. Here too, our MC simulations predicted no influence of the energy broadening on the ion cluster size distributions of the particles.

Our most important physical results shows, for the first time, that different particles of equal LET (average energy deposit) have different stochastic effects at the scales of the DNA. We have found that protons have about 20% higher probability to induce ion clusters of a given size, compared to α-particles of equal LET . The difference arises from the ability of the protons to induce denser ionizations patterns, mainly due to their shorter δ-electrons range. This result reflects the different track-structure of the particles, when examining it on nanometer scales.

Extensive biological experiments of irradiating plasmid DNA and analyzing the induced damage, show that protons have higher biological effectiveness than the α-particles, indicating that

the higher clustering of the ionizations on nanometric scales leads to the production of more lethal damage to the DNA molecule. This demonstrates, for the first time, that the ionization patterns at the DNA scale plays a major role in the determinations of the biological effectiveness of the radiation.
Although the low energy protons suffered energy degradation and scattering, causing the irradiation conditions to differ from those with the α-particles, we believe that we have found solid evidence that the protons are more biologically-hazardous than the equal-LET α-particles, a quality originating from the differences in the particles' track-structure on nanometric scale.
Our MC code, based on the physical model of the radiation interaction and on the mechanisms occurring within the ND, proved to be a very useful tool, having a good correspondence between the measured and simulated ionization patterns; it will be improved when the over-counting phenomenon in the ND would be understood. The MC simulations may be used to predict ionization patterns induced by any mixed radiation fields; these are of prime importance in radiation research nowadays.
My task in this MSc research project was to establish the possible differences in the biological effectiveness of two different particles of equal LET, which was successfully accomplished.
A more extended aim of this research is to develop a biophysical model correlating the physical and biological results. Such model, developed within the Ph.D. thesis of G. Garty, is based on extensive physical and biological measurements in numerous radiation fields.
This model would provide a more accurate evaluation of radiation quality. It will permit better definition of radiation hazards and the development of new, more effective, radiation protection standards and means. But most of all, the more precise knowledge of the influence of the track structure on the biological effectiveness of the radiation, would significantly improve radiation therapy planing, resulting in more accurate and effective cancer treatments.

References

[1] T. R. Munro. The relative radiosensitivity of the nucleus and cytoplasm of chinese hamster fibroblasts. *Radiat. Res.*, 42:451–470, 1970.

[2] R. Iyer and B. E. Lehnert. Effects of ionizing radiation in targeted and nontargeted cells. *Arch. Biochem, Biophys.*, 376(1):14–25, 2000.

[3] ICUR. Linear energy transfer. Technical Report 16, ICUR Publications, 1970.

[4] D.T. Goodhead. Relationship of microdosimetric techniques to applications in biological systems. *The Dosimetry of Ionizing Radiation*, II:1–89, 1987.

[5] M. Belli and D.T. Goodhead. Direct comparison of biological effectiveness of protons and alpha-particles of the same LET. II. mutation induction at the hprt locus in v79 cells. *Int. J. Radiat. Biol.*, 61(5):625–629, 1992.

[6] O. Sapora M. Belli F. Ianzin and M.A. Tacocchini. DNA double strand break production and rejoinig in V79 cells irradiated with light ions. *Adv. Space Res.*, 18(1/2):73–86, 1996.

[7] G. Taucher-Scholz G. Kraft B. Michaeland and M. Belli. The in-flux of nuclear science to radiobiology. Technical report, NuPECC.

[8] E. Friedberg G. Walker and W. Siede. *DNA repair and mutagenesis.* Blackwell, 1995.

[9] F. Cucinotta, editor. *Cellular and tissue response to radiation damage*, volume 2. Space radiation health newsletter, 2002.

[10] S. Powell and T.J. McMillan. DNA damage and repair following treatment with ionizing radiation. *Radiother. Oncol*, 19:95–108, 1990.

[11] J.F. Ward. DNA damage produced by ionizing radiation in mammalian cells. *Prog. Nucl. Acid and Molec. Biol.*, 35:95–125, 1988.

[12] M. F. Rettberg U. Klimczak, D.C. Ludwig. Irradiation of plasmid and phage dna in water-alcohol mixtures: strand breaks and lethal damage as a function of scavenger concentration. *Int. J. Radiat. Biol.*, 64:497–510, 1993.

[13] J.W.T Spinks and R.J. Woods. *An introduction to radiation chemistry.* John Wiley, 1965.

[14] A.J. Swallow. *Radiation chemistry - an introduction.* Halsted press, 1973.

[15] M. Dizdaroglu. Measurements of radiation-induced damage to DNA at the molecular level. *Int. J. Radiat. Biol.*, 61(2):175–183, 1992.

[16] D.J. Brenner and J.F. Ward. Constraints on energy deposition and target size of multiply damaged sites associated with DNA double-strand breaks. *Int. J. Radiat. Biol.*, 61(6):737–748, 1992.

[17] E.J. Kobetich and R. Katz. Energy deposition by electron beams and δ-rays. *Phys. Rev.*, 170(2):391–396, 1968.

[18] F Sauli. Principles of operation of multiwire proportional and drift chambers. Technical report, CERN, 1976.

[19] E.L. Alpen. *Radiation biophysics*. Academic press, 1998.

[20] H.H. Rossi W. Rozenzweig. A device for the measurements of dose as a function specific ionization. *Radiobiology*, 64:404–411, 1955.

[21] D.E. Charlton H. Nikjoo and J.L. Humm. Calculation of initial yields of single- and double-strand breaks in cell nuclei from electrons, protons and alpha particles. *Int. J. Radiat. Biol.*, 56(1):1–19, 1989.

[22] R.W. Shulte. Development of nanodosimetry for biomedical applications. Project progress report, 1998.

[23] U. Fano. Note on the bragg-gray cavity principle for measuring energy dissipation. *Rediat. Res.*, 1:237–240, 1954.

[24] A.J Walker. Principles of experimental microdosimetry. *Radiat. Prot. Dosim.*, 61(4):297–308, 1995.

[25] B. Grosswendt. Formation of ionization clusters in nanometric structures of propane-based tissue-equivalent gas or liquid water by electrons and α-particles. *Radiat. Environ. Biophys.*, 41:103–112, 2002.

[26] G. Garty S. Shchemelinin A. Breskin R. Chechik and G. Assaf. The performance of a novel ion-counting nanodosimeter. *Nucl .Inst and Meth. A*, 492:212–235, 2002.

[27] S. Shchemelinin A. Breskin R. Chechik A. Pansky P. Colautti V. Conte L. De Nardo and G. Tornielli. Ionization measurements in small gas samples by single ion counting. *Nucl. Instr. and Meth. A*, 368:859–861, 1996.

[28] S. Shchemelinin A. Breskin R. Chechik A. Pansky and P. Colautti. A nanodosimeter based on single ion counting. *Microdosimetry - An interdisciplinary approach*, pages 375–378, 1997.

[29] D.T. Goodhead and M. Belli. Direct comparison of biological effectiveness of protons and alpha-particles of the same LET. I. irradiation methods and inactivation of synchronous v79, hela and c3h 10t cells. *Int. J. Radiat. Biol.*, 61(5):611–624, 1992.

[30] S. Shchemelinin A. Breskin R. Chechik P. Colautti and R.W.M. Schulte. First measurements of ionisation clusters on the DNA scale in a wall-less sensitive volume. *Radiat. Prot. Dosim.*, 82(1):43–50, 1999.

[31] B. Grosswendt and W.Y. Baek. Basic physical data in organic gases. INFN 161, Radiation Quality Assessment Based on Physical Radiation Interaction at Nanometer Level, 2000.

[32] J.F. Ziegler J.P. Biersack and U. Littmark. *The Stopping and Range of Ions in Solids.* Pergamon Press, New York, 1985.

[33] L.A. Lewis and J.J. Opplt, editors. *Handbook of Electrophoresis.* CRC press, 1980.

[34] L.H. Lutze and R.A. Winegar. pHAZE: a shuttle vector system for the detection and analysis of ionizing radiation-induced mutations. *Mutat. Res.*, 245:305–310, 1990.

[35] R. Cowan C.M. Collis and G.W. Grigg. Breakage of double-stranded DNA due to single-stranded nicking. *J. Theor. Biol.*, 127:229–245, 1987.

[36] M. Gulston J. Fulford T. Jenner T. deLara and P. O'Nieil. Clustered DNA damage induced by g radiation in human fibroblasts (HF19), hamster (V79-4) cells and plasmid DNA is revealed as fpg and nth sensitive sites. *Nucl. Acids. Res.*, 30:3464–3472, 2002.

[37] A. Tartari E. Casnati and C. Baraldi. An empirical approach to K-shell ionization cross-section by electrons. *J. Phys. B*, 15:155–167, 1982.

[38] C.H. Rutledge and R.L. Watson. Cross section for K-shell ionization by 1H, 2H, 3He ion impact. *Atom. Nuc. data tables*, 12:195–216, 1973.